Magnetic resonance measurements of sub-cellular membrane structures in live and fixed neural tissue

Nathan H. Williamson[1 *], Rea Ravin [1,2 *], Dan Benjamini[1,3], Hellmut Merkle[4], Melanie Falgairolle[4], Michael J. O'Donovan[4], Dvir Blivis[4], Dave Ide[4], Teddy X. Cai[1], Nima S. Ghorashi[5], Ruiliang Bai[6,1], and Peter J. Basser[1] ✉

[1]Eunice Kennedy Shriver National Institute of Child Health and Human Development, National Institutes of Health, Bethesda, MD, USA
[2]Celoptics, Rockville, MD, USA
[3]Center for Neuroscience and Regenerative Medicine, Henry Jackson Foundation, Bethesda, MD, USA
[4]National Institute of Neurological Disorders and Stroke, National Institutes of Health, Bethesda, MD, USA
[5]Cardiovascular Branch, National Heart, Lung, and Blood Institute, National Institutes of Health, Bethesda, MD 20892
[6]Interdisciplinary Institute of Neuroscience and Technology, Qiushi Academy for Advanced Studies, Key Laboratory of Biomedical Engineering of Ministry of Education, College of Biomedical Engineering and Instrument Science, Zhejiang University, Hangzhou, China
[*]N.H.W. and R.R. contributed equally to this work.

We develop magnetic resonance (MR) methods for measuring real-time changes of tissue microstructure and membrane permeability of live and fixed neural tissue. Diffusion and exchange MR measurements are performed using the large static gradient produced by a single-sided permanent magnet. Using tissue delipidation methods, we show that water diffusion is restricted solely by lipid membranes. Most of the diffusion signal can be assigned to water in tissue which is far from membranes. The remaining 25% can be assigned to water restricted within membrane structures in the range of 200–1400 nm at the cellular, organelle, and vesicle levels. Diffusion exchange spectroscopy measures water exchanging between sub-cellular structures and free environments at 100 s^{-1}.

tissue microstructure|diffusion exchange spectroscopy | porous media | membrane permeability| NMR-MOUSE

Correspondence: ***basserp@mail.nih.gov***

Introduction

The first diffusion tensor images of brain tissue showed diffusion anisotropy in the white matter (1). It was postulated that this anisotropy is due to myelin membranes and other cellular components impeding water mobility more in the direction perpendicular to the oriented fibers than parallel to them. By process of elimination, Beaulieu concluded that the origin of diffusion anisotropy in white matter is due to axonal cell membranes (2, 3). New methods to clear lipid membranes while leaving other tissue components intact (4, 5) have confirmed directly that diffusion becomes isotropic and diffusivity approaches the value of free water after complete delipidation (6).

A characteristic of magnetic resonance (MR) is that spin magnetization retains the history of motions encoded during the experimental pulse sequence (7). Diffusion MR measures the spin echo (8) signal attenuation of nuclear spins which displace randomly in the presence of a magnetic field gradient during a defined diffusion encoding time (9–11). Sensitization to smaller and smaller net displacements can be achieved by increasing the gradient strength, duration and/or the diffusion encoding time, and the effect can be summarized in a single variable, b (12). The diffusion MR signal from a single species such as freely diffusing water with self-diffusion coefficient D_0 attenuates as $\exp(-bD)$(13), while water diffusing within restricted environments attenuates more slowly (14–18). The diffusion MR signal of water in heterogeneous materials such as biological tissue would be expected to contain a multitude of components arising from water in different microenvironments, which restrict water diffusion to varying degrees (19).

Investigation of neural tissue using diffusion MR has led to numerous reports of two dominant diffusivity regimes. As a result, a biexponential model, which assumes that the signal is a sum of two components with distinct diffusion coefficients (20–22), has been used to fit the water diffusion signal attenuation. Albeit simple, a two-component model cannot capture the complexity and heterogeneity of the underlying microstructure of biological tissue. With the advent of model-independent empirical data inversion techniques, the diffusion signal attenuation could be described by a distribution of diffusion coefficients (23), a phenomenological representation which makes no assumptions about tissue microstructure (24). This study, along with more recent ones (25, 26), suggest that the diffusion coefficient distribution can be used to investigate the microstructural properties of neural tissue.

Nuclear spins may also exchange along the diffusion coefficient distribution by moving between microenvironments, causing diffusion coefficients of components to shift and appear closer together on the distribution. Exchange can be measured from the change in apparent diffusion coefficients with encoding time (27–30). Alternatively, MR can store the spin history from one encoding b_1 during a mixing time t_m and recall it for a second encoding b_2 to measure exchange along the distribution (31). The standard diffusion measurement is one-dimensional (1-D) in that there is one encoding variable b and one measured parameter D. By encoding the spins twice (b_1, b_2), the diffusion exchange spectroscopy (DEXSY) sequence becomes 2-D (31). 2-D DEXSY measures the relationship between spins' diffusion coefficients at two separate instances (D_1, D_2) to show exchanging and

non-exchanging components (32, 33).

The full DEXSY sampling of the 2-D $b_1 - b_2$ space (31) is too time-consuming for scanning live specimen. Recent research shows that there is some redundancy in the data (33–36) and alternative DEXSY-based approaches may measure exchange with fewer data points (33, 37, 38). Cai, et al., developed a rapid measurement of f from just four points in the $b_1 - b_2$ space (38).

Larger gradients, pulse durations, and encoding times probe smaller structures (10). Hardware constraints cap the maximum strength of gradient coils of MR microimaging systems at a few Tesla/m. With long pulse durations and encoding times, Diffusion MR microstructural resolution is predicted to be limited to structures larger than a micron(39). However, when water pools communicate during encoding, signal components become blurred, further limiting resolution. Gradients are pulsed for at least a millisecond, which sets a lower limit for the encoding time (40). Surprisingly, an experiment dating back to the origins of MR (8, 9), performed in a large static gradient field, can break this microstructural resolution limit (41). Low-cost, portable, bench-top, single-sided NMR devices with greater than 10 T/m static gradients (42) can probe sub-micron structures (43) that ordinarily cannot be resolved from larger microscale structures using state-of-the-art pulsed gradient MR systems with lower maximum gradient strengths (44). Displacement encoding within a static gradient field occurs by using radiofrequency (RF) pulses (8, 9) to switch the "effective gradient" (11), allowing for diffusion encoding times as short as 100 μs (45). This permits resolution of sub-micron structures that can contain rapidly exchanging water pools (43). The static gradient 1-D diffusion (46) and 2-D DEXSY (47) experiments can then be used to probe cellular and sub-cellular components and water exchange between and among them.

In this paper we adapt 1-D diffusion and 2-D diffusion exchange methods to perform measurements with a single-sided MR system having static gradients, to investigate the cellular and sub-cellular structures in isolated newborn mouse spinal cord. We develop a system to support both live and fixed spinal cords during NMR measurements such that data could be compared directly. For this reason, all experiments performed on fixed tissue in this paper use protocols designed for live specimen. Diffusion coefficient distributions show signal from water in various restricted environments. Diffusion signal attenuation can separate restrictions in the window of 200–1400 nm, indicating that sub-cellular structural resolution is achieved. DEXSY reveals the water pools that exchange between restricted and free environments on a timescale of 10 milliseconds, indicating that sub-cellular membrane structure can only be measured with encoding times less than 10 ms. Replacing the protons of water with deuterium (D_2O) decreased the signal from all components of the distribution equally, indicating that the majority of the signal is coming from water. Delipidation of membranes by the surfactant Triton X indicated that restriction was caused by lipid membranes and not proteins.

Results

1-D diffusion measures 25% of water to be restricted. Signal was acquired over an entire region including the spinal cord sample and artificial cerebro-spinal fluid (aCSF) bathing the sample. The contribution from the aCSF surrounding the sample needed to be quantified. Fig. 1 shows distributions of diffusion coefficients for a fixed spinal cord bathed in aCSF (a) and after removing the aCSF (b). These can be compared to the distribution from only aCSF filling the RF coil (c). Differences in the fraction of the most mobile diffusion coefficient component (integral of $P(D/D_0)$ for $D/D_0 > 0.17$) indicates that aCSF accounts for only 5% of the signal in (a). The solenoid coil itself does an excellent job isolating signal from the tissue. Comparing the distributions in (a) and (b) demonstrate that the solenoid RF coil gets signal from the spinal cord specimen filling its interior (see Methods)).

Diffusion coefficients are nondimensionalized by the diffusion coefficient of aCSF $D_0 = 2.15 \times 10^{-9}$ m^2/s found by monoexponential fits (see supporting information (SI) Fig. S1). aCSF is well described by a single diffusion coefficient and thus its distribution should be a delta function at $D/D_0 = 1$. However, data inversion yields a smooth, broad distribution because of regularization, which is needed to stabilize distribution estimates (48).

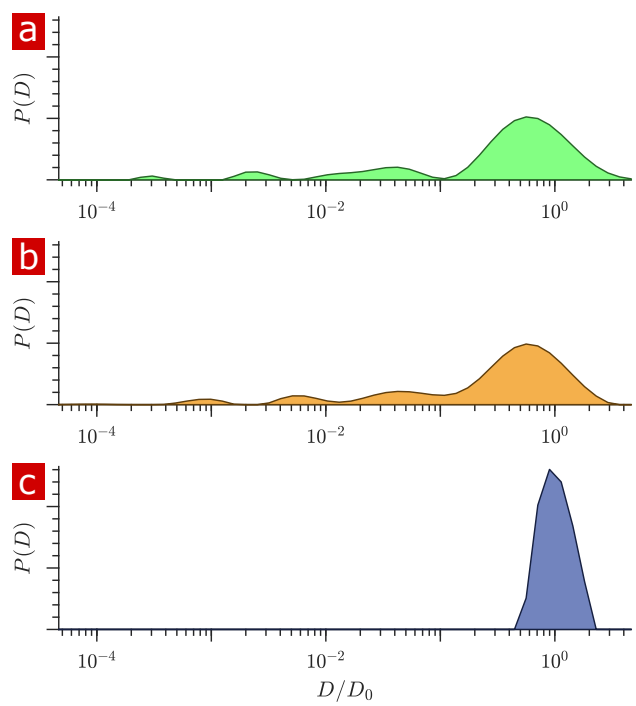

Fig. 1. Diffusion coefficient distributions of a fixed spinal cord bathed in aCSF (a), without aCSF (b), and of only aCSF filling the RF coil (c).

Signal attenuation and diffusion coefficient distributions from 1-D diffusion measurements performed on a fixed spinal cord specimen are presented in Fig. 2. Signal attenuation from measurements of pure aCSF is also shown for comparison. Attenuation models are used to define signal and distribution components as free (13), localized near surfaces but not completely restricted (17, 18) and restricted (14–16)

(described in the SI Appendix). Signal is plotted as a function of the non-dimensionalized diffusion encoding variable $b \times D_0$. Exponential attenuation is expected for fluids diffusing freely, as shown by Eq. S1. N.B. The largest b corresponds to 3,000,000 $\mathrm{s/mm^2}$, two to three orders of magnitude larger than what is typically reached in conventional pulsed gradient diffusion MRI studies. aCSF signal is monoexponential and quickly attenuates to the background noise level. Spinal cord signal attenuation is multiexponential over the entire range of b and does not fully attenuate, implying the presence of multiple highly restricted pools.

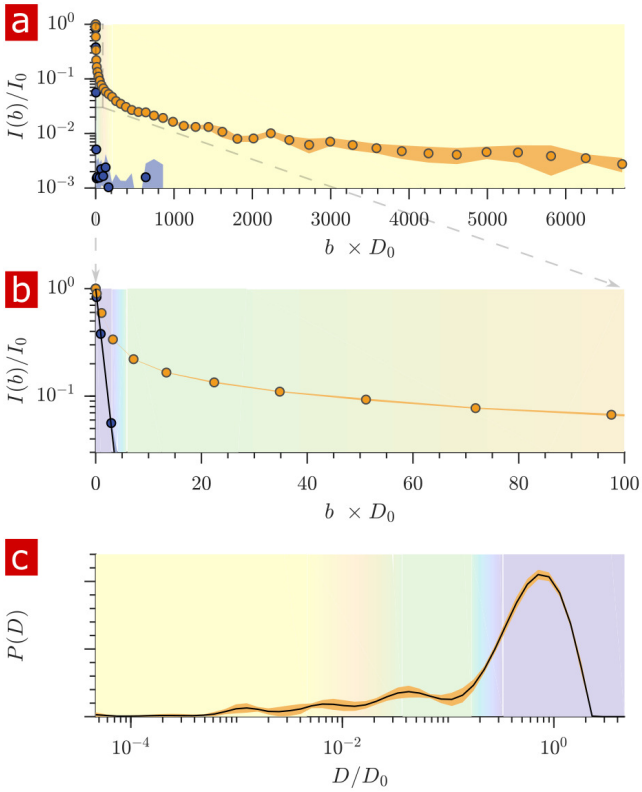

Fig. 2. a,b) Mean (circles) and standard deviation (shaded bands) of the signal intensity from five diffusion measurements, spaced 54 minutes apart, performed on a fixed spinal cord (orange) and three measurements performed on aCSF (purple) at 25°C. In (a) and (b) (showing the initial attenuation), the signal intensity is plotted as a function of $b \times D_0$ where $D_0 = 2.15 \times 10^{-9}$ $\mathrm{m^2/s}$ is the diffusion coefficient obtained from monoexponential fits of the aCSF. c) The distribution of diffusion coefficients resulting from inversion of the data. The purple, green, and yellow shading across plots signifies water which is free, localized, and restricted respectively. The color gradient is meant to signify a continuous change between diffusion regimes rather than sharp boundaries.

The distribution of apparent diffusion coefficients is shown in Fig. 2 (c). The majority of the distribution has $D/D_0 > 0.3$, and this is labeled the free water component. Humps extend to lower values of D/D_0 and these represent signal which is more and more restricted and on smaller length scales, as indicated by the color gradient.

Full DEXSY measures water exchanging between free and restricted environments 100 times per second. 2-D DEXSY labels spins based on their local mobility at two instances which are separated by the mixing time variable t_m (31). This permits the direct measurement of water movement from one environment (e.g. A) to another (B) as well as water moving in reverse (B) to (A) to fulfill mass conservation. In the case that water exchanges between environments on intermediate timescales (greater than the diffusion encoding time and less than the longitudinal relaxation time T_1 which causes spins to forget their encoding), the exchange increases and saturates as a function of t_m (33, 38, 49, 50). The classic analysis of DEXSY is as a joint 2-D probability distribution showing relationships between the apparent diffusion coefficients of water populations during the first encoding period, D_1 and the second encoding period D_2 (33). Integrated probability density at a point or region (D_1, D_2) indicates the probability of a spin being at D_1 during encoding 1 and D_2 during encoding 2. Non-exchanging water populations have $D_1 = D_2$, defining a diagonal line across the distribution whereas exchanging water populations are located off the diagonal. A representative 2-D DEXSY distribution of spinal cord is shown in Fig. 3 (a). The distribution is divided into a 3x3 grid for the possible exchange pathways between components A ($3.2 \times 10^{-4} - 1 \times 10^{-2}$), B($1 \times 10^{-2} - 3.2 \times 10^{-1}$), and C ($5.6 \times 10^{-1} - 10$), shown by the color coding and labels. The integrated probability density from each region represents an exchange (off-diagonal) or non-exchange (on-diagonal) fraction. The distribution shows exchange between free water, labeled as C and restricted water, labeled as B and A. Additionally, there appears to be exchange between restricted components. Stacked plots at $t_m = 0.2$, 4, 20, and 160 ms (b) show the increase in probability for components exchanging with free water, regions $\mathrm{AC} + \mathrm{CA}$ and regions $\mathrm{BC} + \mathrm{CB}$ and a decrease in probability for the non-exchanging components, e.g., region AA appears to decrease to near zero at the longest t_m.

Fig. 4 shows exchanging (a) and non-exchanging (b) fractions, f from integrating regions of the 2-D probability distributions. The build-up (a) and decay (b) of f over t_m are fit with a first order rate equation to obtain apparent exchange rates (AXRs), presented in the figure caption. Measurements on six different spinal cords show consistent exchange behavior. Restricted components exchange with free water with AXR$\approx$100 $\mathrm{s^{-1}}$. $f_{\mathrm{AB+BA}}$ does not increase with t_m, indicating that the DEXSY measurement is primarily sensitive to water exchanging between restricted and free environments and not between and among different restricted environments.

Rapid exchange measurement agrees with full DEXSY. Full DEXSY measurements at four mixing times took eight hours—too long to measure exchange in living tissue. Therefore, we strove to develop a method to rapidly measure exchange (38) (see SI). The rapid measurement provides an apparent exchange fraction f, a diffusion-weighted average of exchange between all water pools. The full DEXSY can resolve multiple exchanging water pools and the exchange pathways between them (51). Although the rapid measurement lacks the full DEXSY's resolution of multi-component exchange, it provides enhanced temporal resolution, both with respect to t_m and experimental time, by side-stepping the need for 2-D data inversion and by acquiring the data much more rapidly. The protocol used here acquired the data

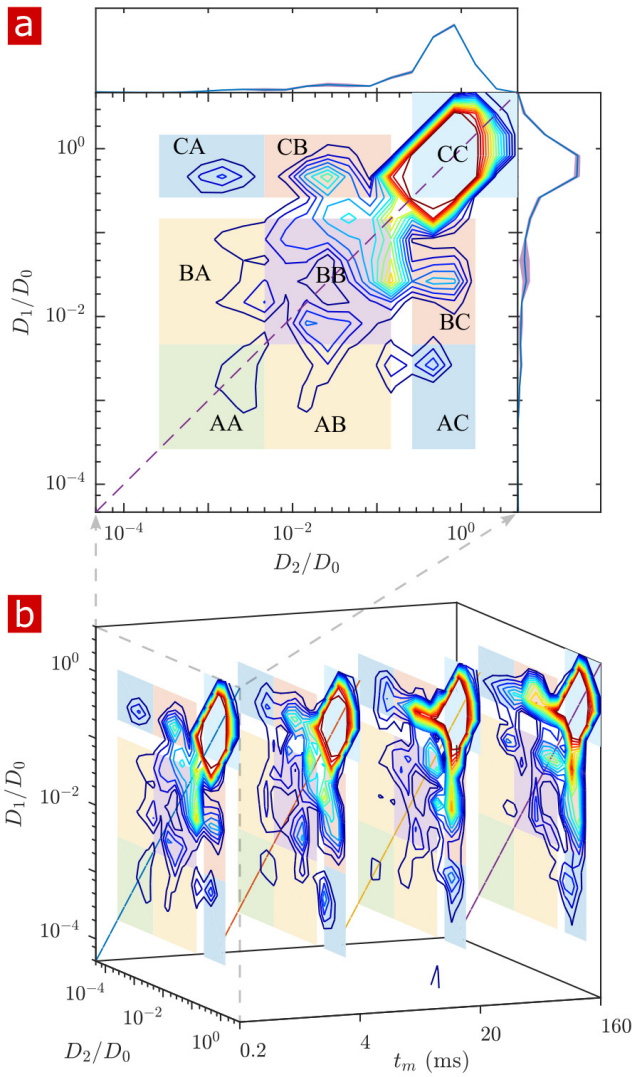

Fig. 3. Full 2-D DEXSY diffusion exchange distribution for a fixed spinal cord at (a) $t_m = 0.2$ ms and (b) $t_m = [0.2, 4, 20, 160]$ ms showing exchanging (off-diagonal) and non-exchanging (on-diagonal) components. These components are lumped into regions A, B, and C, shaded and labeled in a 3×3 grid for each exchange combination. The range of $P(D_1, D_2)$ is set to add detail to components A and B, but cuts off the top of the most mobile region CC. In (a), the marginal distributions $P(D_1)$ and $P(D_2)$ are presented on the sides, with means (solid blue lines) and standard deviations (shaded regions) from 3 measurements. With increasing t_m, (b) shows the build-up of the probability density in regions of free and restricted water exchange $\mathrm{AC}+\mathrm{CA}$ and $\mathrm{BC}+\mathrm{CB}$ and the decay of the non-exchanging restricted water regions AA and BB. The build-up and decay is quantified in Fig. 4.

for one exchange fraction (one mixing time) per minute. Exchange fractions from the rapid measurement are presented in Fig. 5 for the same specimen as used for the full DEXSYs (Figs. 3 and 4). The AXR from three repeat measurements was 110 ± 30 s^{-1}. This value is not different statistically from the results of the full DEXSY measurement, validating the rapid measurement method. Additionally, the value from repeated measurements on five samples was 110 ± 6 s^{-1} at 25°C, indicating high reproducibility.

Restricted diffusion measures sub-micron structures. After free water has fully attenuated, restricted water signal attenuation is exponential with the diffusion encoding time τ (14–18), as presented in Eqs. S2–S4. Attenuation models

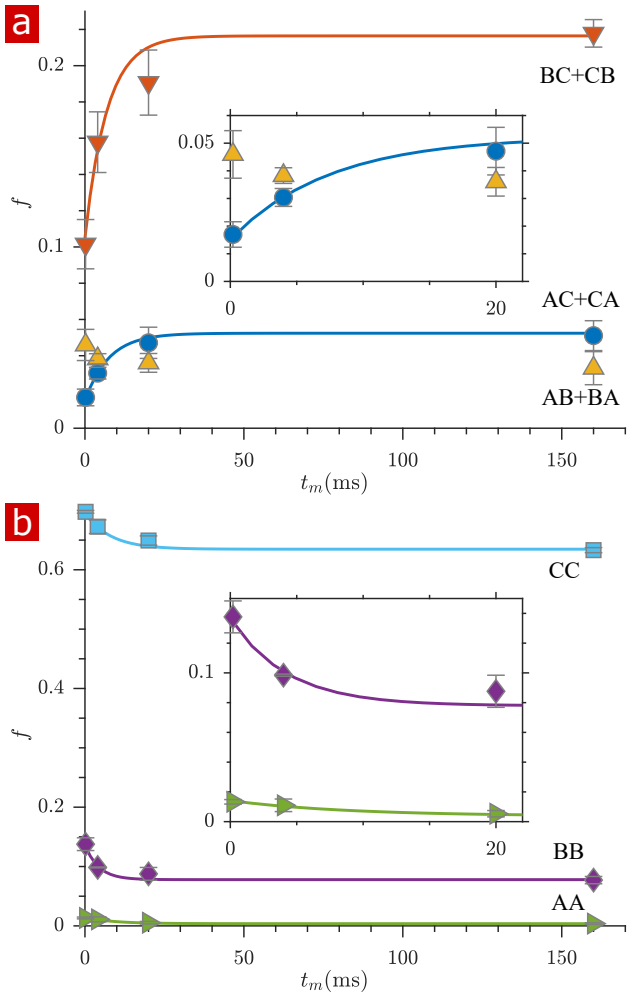

Fig. 4. Fractions of exchanging (a) and non-exchanging (b) spins between regions A, B, and C, defined in Fig. 3. a) Exchanging fractions $f_{\mathrm{AC+CA}}$ and $f_{\mathrm{BC+CB}}$ build up and plateau. Fits with a first-order rate model estimated apparent exchange rates AXRs (mean±standard deviation from three measurements) 140 ± 80 and 140 ± 140 s-1 respectively. $f_{\mathrm{AB+BA}}$ does not follow the expected first order rate model. b) Non-exchanging fractions f_{AA}, f_{BB}, and f_{CC} also follow a first order rate model with estimated AXRs 110 ± 100 , 230 ± 170 , and 130 ± 100 s-1 respectively. Insets zoom in on the initial changes of f. Error bars are the standard deviations from three repeat measurements.

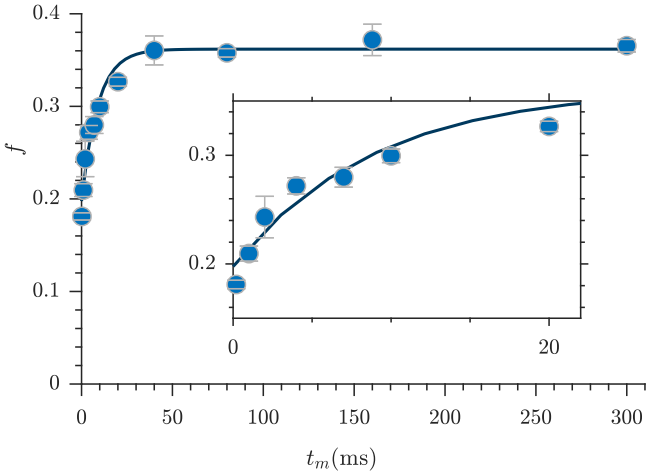

Fig. 5. Rapid measurement of exchange fractions and fit (estimated AXR = 110 ± 30 s-1). Inset shows a zoomed-in region of the bottom left corner of the plot.

for water restricted in spheres of radius R indicate that with $g = 15.3$ T/m the diffusion experiment provides a 200–1400 nm window on restriction radii (Fig. 6 (a)). Signal from water in restrictions smaller than $R = 200$ nm does not attenuate significantly enough to differentiate. In restrictions larger than R=1400 nm, signal from water far from the surfaces attenuates as free water and signal from water near the surface attenuates as localized water (restricted on one side but free on the other). The long time behavior of the diffusion signals are analyzed to estimate a radius of restriction in Fig. 6 (b). Exchange also causes attenuation which is exponential with τ (43). The estimate accounts for attenuation due to exchange, utilizing the measured AXR. The estimated radius is $R = 900$ nm. This can be viewed as a volume-averaged restriction length, filtering out water in structures with $R > 1400$ nm.

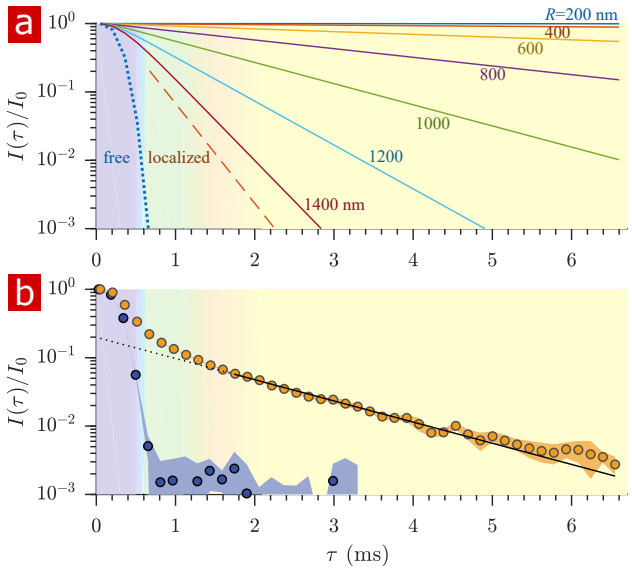

Fig. 6. Diffusion signal intensity as a function of the variable τ (rather than $b \sim \tau^3$), (a) simulated, and (b) experimental, re-plotted from Fig. 2. (a) Signal is simulated for water restricted in spherical compartments (Eq. S3) (16) of varying radius between $R = 200 - 1400$ nm (solid lines), for water localized near a surface in larger restrictions (Eq. S2, dashed line) (17, 18), as well as water diffusing freely (Eq. S1, dotted line) (13). (b) The solid line is a fit of the signal at $\tau \geq 1.8$ ms with the model for water restricted in spherical compartments in the limit of long τ (Eq. S5) (16) incorporating the AXR=110 s^{-1} (43), estimating a radius $R = 900$ nm. The dotted line extrapolates back to $I/I_0 = 0.2$. The deviation from monoexponential attenuation at long times is due to microstructural heterogeneity within the sample.

NMR recordings do not affect viability of spinal cord. The signal attenuation from diffusion measurements performed on live spinal cords (n=9) is compared to that of fixed (n=6) and aCSF in Fig. 7 (a). The signal attenuates slightly faster although not significantly as seen by the standard deviations. The mobility of water on the timescale of milliseconds is very similar in live and fixed specimen.

After two hours of NMR measurements and four to seven hours post-dissection, viability of spinal cords (dissected on postnatal (P) day P2, P3, and P4) was assessed by recording motoneuronal electrical activity after stimulation of a dorsal root. Mono- and polysynaptic reflexes were recorded in all preparations (n=4), Fig. 7 (b), indicating that neither the experimental setup nor the protocol compromised the neuronal excitability of the spinal cord.

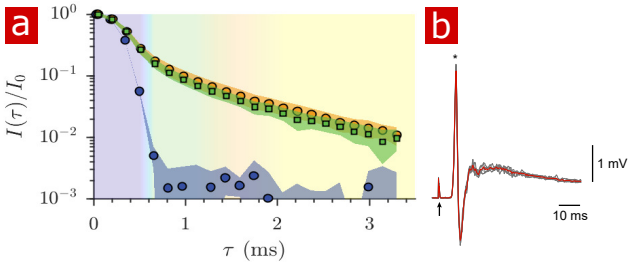

Fig. 7. Signal intensity from diffusion measurements performed at $25°C$ on live samples (n=9) (green squares), fixed samples (n=6) (orange circles) and aCSF (blue circles) plotted as a function of the variable τ. (b) Mono- and poly- synaptic reflexes were recorded from the L6 ventral root of live samples (n=4) after NMR measurements. Stimulation was done on the homonymous dorsal root. The grey lines are 5 successive stimuli (30s interval) and the superimposed red line is the average signal. The arrow indicates the stimulus artifact and the star the monosynaptic reflex.

NMR measurements are primarily sensitive to water. To determine whether biomacromolecules were contributing to the signal observed in the spinal cords, rapid exchange and 1-D diffusion measurements were recorded in real-time as a specimen was washed with aCSF made with 99.8% deuterium water (D_2O aCSF). (Results are presented in Fig. S2). After two successive washes, proton signal decreased to values similar to D_2O aCSF alone. All diffusion coefficient distribution components decreased similarly after D_2O washing. Components of the distribution which are not from water would still remain after removing H_2O. Therefore, all distribution components are primarily made up of water. This points to water rather than biomacromolecules accounting for the vast majority of the measured signal.

Delipidation shows membranes to be the sole source of restriction. Triton X surfactant was used to remove lipid membranes from spinal cords in order to determine the effect of membranes on water restriction. The aCSF bathing the spinal cord was replaced with aCSF with Triton X while rapid exchange and 1-D diffusion measurements were repeatedly performed (n=2). Fig. 8 shows exchange fractions (a) and 1-D distributions from select time points (b).

After the addition of 1% Triton X at 1 hr, the exchanging fractions decreased slowly and reached a plateau. Washing to 5% Triton X at 50 hrs decreased the exchange fractions further until they again reached a plateau.

The diffusion coefficient distributions Fig. 8(b) (and SUP. VIDEO S1) show that the delipidation process removed the barriers for restriction. Therefore, lipid membranes, not the remaining macromolecules, are the source of restriction of water diffusion. The fraction of restricted water (Fig. S3) decreases and plateaus similarly to the exchange fractions.

About 6% of the signal appears restricted after 120 hrs of delipidation. This is signal from the protons on Triton X, which as a 5% solution imparts a 6% signal at $D/D_0 = 0.01$ (see Fig. S4).

Samples were also studied after full delipidation and washing away Triton X (Fig. 9). The diffusion signal attenuation,

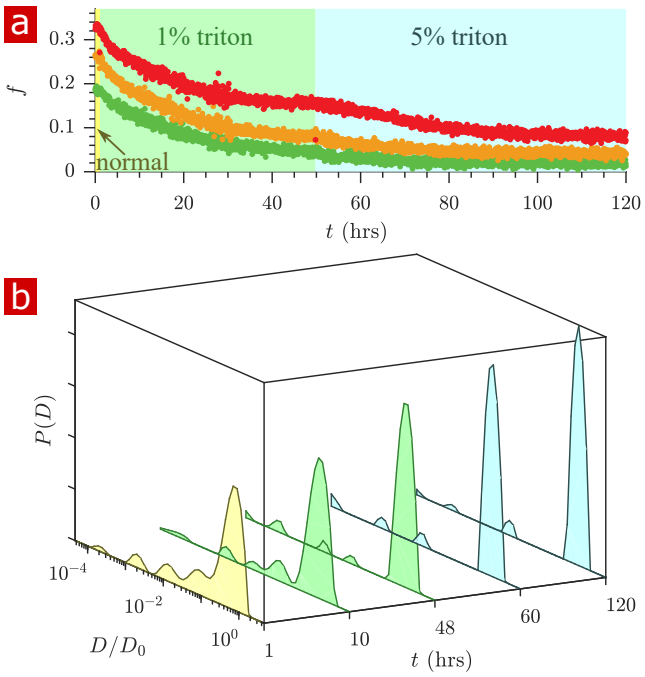

Fig. 8. Timecourse study of Triton X delipidation, in which the sample was washed to aCSF with 1% Triton X, and then 5% Triton X showing (a) exchanging fractions from rapid exchange measurements with $t_m = 0.2$ (green), 4 (orange), and 20 ms (red), and (b) representative distributions throughout the timecourse.

(a) and (b), shows that 95% of the signal is monoexponential with $D/D_0 = 0.90$. The diffusion coefficient distribution (c) shows one major free diffusion peak which is not significantly different from the diffusion coefficient distribution of pure aCSF. Some small peaks which are not seen unless $P(D)$ is magnified lead to a 1% restricted component. Without membranes there is essentially only one diffusive environment throughout the whole sample.

Discussion

We present diffusion data which uses water to probe cellular and sub-cellular membrane structures on sub-millisecond and millisecond timescales. Much of the advance was possible because the large static gradient overcomes (41) many hardware (40) (e.g. slew rate, eddy currents, maximum gradient strength) and biological (e.g. peripheral nerve stimulation (52)) limitations of pulsed gradients. In 1996 Köpf, et al., realized this capability on biological tissue, performing diffusion measurements using a 50 T/m static gradient in the stray field of a superconducting 9.4 T magnet (53). Another stray field study by Carlton, et al., (43) used an 18 T/m static gradient to measure bacteria concentrations. Bacteria cell membranes are roughly a micron in diameter, similar to sub-cellular structures in tissue. They noted the static gradient experiment provided more intracellular signal compared to pulsed gradient experiments on bacterial systems(44) due to less exchange during the shorter diffusion encoding time. We re-purposed a low field single-sided permanent magnet (42) which, due to its profiling capabilities (54), has found a number of niche applications in materials science and engineering, biology and medicine, and cultural heritage (55–57).

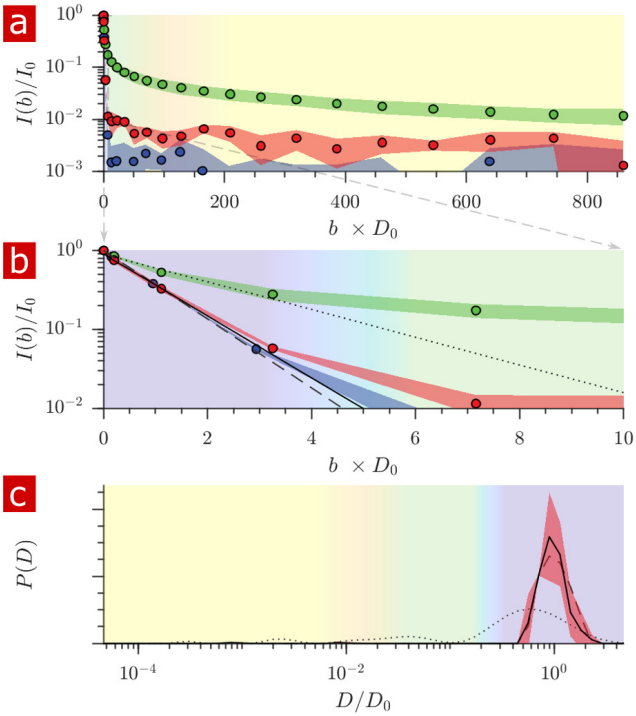

Fig. 9. a,b) Diffusion signal intensity and (c) distribution from measurements on spinal cords performed at 25°C after delipidation (n=2) with 10% Triton X and washing. The mean (circles) and standard deviation (shaded region) of the attenuation are plotted for the delipidated samples (red) alongside pure aCSF (purple) and fixed undelipidated spinal cords (n=6) (green). The initial attenuation (b) of the delipidated samples looks very similar to pure aCSF. Monoexponential fits of the attenuation from points 2–4 yielded 2.15 ± 0.01, 1.94 ± 0.02 and $0.87 \pm 0.14 \times 10^{-9}$ m^2/s for the aCSF, delipidated, and undelipidated spinal cords and are shown as the dashed, solid, and dotted lines respectively. Diffusion coefficient distributions (c) of the undelipidated spinal cords, for which the mean (solid line) and standard deviation (shaded region around line) are not significantly different from the pure aCSF (dashed line). The distribution from a fixed, undelipidated spinal cord (dotted line) is also shown for comparison. The purple, green, and yellow shading across the plots signifies water which is free, localized, and restricted.

The large 15.3 T/m gradient allowed for the attenuation of signal below $I/I_0 = 0.01$ in a diffusion encoding time of 6.6 ms.

A large signal-to-noise ratio (SNR) and Gaussian zero mean noise was needed to resolve slowly attenuating signals above the noise and to not confuse the signal with a baseline noise floor. In general, SNR > 100 is needed for diffusion coefficient distribution analysis (58) and as a rule-of-thumb this allows for resolution of populations comprising as little as 1% of the signal. Performance tuning led to very stable measurements and SNR > 600. These modifications included a 2000 echo CPMG readout, 25 μs echo time, a sample-specific solenoid RF coil, a wet/dry chamber without circulation, and noise reduction/isolation.

The solenoid RF coil permitted low-power, 2 μs RF pulses, high filling factor, and maximized signal from the spinal cord filling its interior relative to aCSF. Previous studies on live ex-vivo neural tissue utilized MR imaging (30, 59–63). However, their analysis was on regions of interest (ROIs) which encompassed the entire sample, indicating that no additional specificity was obtained from the imaging. Because 95%

of the signal came from spinal cord tissue, we did not need imaging. This let us achieve high SNR and sufficiently rapid measurements.

The wet/dry chamber kept the liquid environment still while the gas environment provided oxygenation. Previous diffusion MRI studies on live ex-vivo neural tissue provided oxygen to the sample through perfused aCSF (30, 59–64). Researchers typically implemented start-stop diffusion MR protocols, with aCSF perfusion between MR measurements (61, 62). This method of pulsed oxygen delivery was able to maintain live tissue based on stable diffusion MR measurements. However, a steady concentration of oxygen is preferable and better represents the in-vivo environment. The wet/dry chamber allowed for a constant supply of oxygen while still obtaining very stable diffusion measurements free of flow artifacts, ideal for diffusion measurements on live tissue. We also directly demonstrate that spinal cords are alive after hours of NMR measurements by recording electrical responses.

Our novel experimental setup reveals signal from highly restricted pools. We determined that these pools are exclusively membrane-restricted water. Previous nerve tissue studies reported two (1-D encoding (23, 25, 26)) and three (2-D, integrated diffusion-relaxation (19)) resolvable water mobility components, spanning 2 orders of magnitude. Here, distributions of diffusion coefficients showed components that are 3 orders of magnitude lower than free water. Similar values have been reported for other, larger, proton bearing molecules naturally occurring in biological tissue (65). However, by replacing the water in the tissue with deuterated water, we determined our methods to be sensitive primarily to water and not macromolecules.

Delipidation showed directly that the decreased mobility of water in tissue is due to restriction by lipid membranes. After full delipidation, the free water peak of the diffusion coefficient distribution accounts for 99% of the water (Fig. 9), vs. roughly 75% of the water before delipidation. A fit of the initial signal attenuation to estimate the mean diffusion coefficient $\langle D \rangle$ showed $\langle D \rangle / D_0 = 0.90$, vs. 0.40 before delipidation. Deviation from monoexponential free diffusion attenuation is due to restriction by lipid membranes.

After removing restrictions, hindrances to water diffusion can be thought of as arising from volume obstruction by macromolecules such as proteins within the tissue. Obstruction models of water (solvent) self-diffusion incorporate only the volume fraction of macromolecules, θ, as a free parameter and are generally adequate models in the limit of low (< 0.1) volume fraction (66). Such models predict $0.03 < \theta < 0.07$ for $\langle D \rangle / D_0 = 0.90$. Neural tissue consists of 8% proteins (6) and thus can account for the obstruction effects. Leuze, et al. used another lipid clearing method to determine that lipids are the dominant source of MRI contrast. We can now additionally say that proteins act as simple obstructions, reducing water diffusion only slightly from D_0. This finding can be compared to previous reports of water diffusion in cytoplasm isolated from red blood cells, showing $\langle D \rangle / D_0 = 0.70$ (67). Although we used shorter diffusion encoding times, delipidated samples showed monoexponenital diffusion signal attenuation with b, indicating that microstructural information is averaged out during the encoding time and should show no additional encoding time dependence (68). The decreased diffusivity from cytoplasm (67) could arise from the presence of organelles and membrane particles still present in the supernatant after lysing and centrifuging the red blood cells.

The static gradient diffusion measurement provides a window on structures in the range of 200–1400 nm. Such structures within neural tissue include cells and portions of cells with small radii such as axons, myelin, dendrites and dendritic spines, and a number of membranous organelles such as mitochondria, endoplasmic reticulum, and vessicles (69). Static gradient methods methods are complementary to pulsed gradients, which provide enhanced resolution to micron-sized cell membrane restrictions, but are unable to attenuate signal from sub-micron cells and organelles (70, 71).

Full 2-D DEXSY distributions showed restricted water exchanges with free water, but could not resolve exchange between restricted water pools. The rapid measurement was designed to hone in on the exchange between restricted and free water pools and AXRs were consistent with results from the full DEXSYs. Results indicate that we have developed a non-invasive, sufficiently rapid method of measuring exchange across membranes in live tissue. The $AXR \approx 100\ \mathrm{s}^{-1}$ is significantly faster than intracellular–extracellular water exchange rates measured in neural tissue ($\approx 1-2\ \mathrm{s}{-1}$) (72–75). Such fast turnovers are not unheard of, e.g. red blood cells show similar ($\approx 100\ \mathrm{s}{-1}$) rates (27, 28, 30) due to their high expression of aquaporin (76). In addition to membrane permeability, the other factor controlling the rate of water turnover is the volume of water within the membrane. Smaller volumes naturally lead to higher turnover rates. Therefore fast AXRs can be explained by the small volumes of the structures which the measurement is sensitive to.

The methods were used to follow penetration of deuterated water into the tissue as well as the delipidation of the tissue via Triton X. The timescale of water penetration was ≈ 1 min, consistent with mass transport theory, but the timescale of Triton X penetration and delipidation was ≈ 1 day, longer than predicted (≈ 3 hrs) (see SI). An increased time is expected due to the reaction front which develops as Triton X delipidates, slowing its overall penetration.

Previous studies addressing the microstructural resolution limit of diffusion MR treated the problem as solely limited by gradient strength (39). The fast exchange rates measured in the current work indicate that resolution is limited by the diffusion encoding time in addition to the maximum gradient strength; exchange cannot be neglected.

Methods

Test chamber and experimental conditions. The experimental test chamber (Fig. 10(a)) was designed to support live spinal cord for hours without requiring oxygenated artificial cerebro-spinal fluid (aCSF) flow, thus avoiding flow-related measurement artifacts. In order to compare data be-

tween live and fixed tissue we used oxygenated aCSF as the buffer solution for all experiments. To achieve this we designed a gas-tight wet/dry chamber that was fabricated at the NIH/NINDS mechanical workshop. The assembled chamber had two environments—a static liquid environment with aCSF and above it a gas environment with a slow flow of humidified 95% O_2 and 5% CO_2 gas. The sample temperature can be controlled in the range of $7-37°C$. Sample temperature was monitored by a PicoM fiber optic sensor (Opsens Solutions Inc., Québec, Canada) and regulated by a shallow water bath surrounding the chamber. The bottom portion of the chamber was made of aluminum to provide good heat conduction to the media. (See SI for additional information.) The spinal cord was placed inside the solenoid RF coil within the chamber half-filled with aCSF previously bubbled with 95% O_2 and 5% CO_2. The chamber was sealed and connected to gas flow with humid 95% O_2 and 5% CO_2.

Mouse spinal cord dissection, fixation, and delipidation. All experiments were performed on Swiss Webster wild type (Taconic Biosciences, Rensselaer, NY, USA) between one day after birth to postnatal day 4 and were carried out in compliance with the National Institute of Neurological Disorders and Stroke Animal Care and Use Committee (Animal Protocol Number 1267-18). The mouse spinal cords were isolated and placed in a dissecting chamber perfused with cold Low-Calcium High Magnesium aCSF (concentrations in mM: 128.35 NaCl, 4 KCl, 0.5 $CaCl_2 \cdot H_2O$, 6 $MgSO_4 \cdot 7H_2O$, 0.58 $NaH_2PO_4 \cdot H_2O$, 21 $NaHCO_3$, 30 D-glucose) bubbled with 95% O_2 and 5% CO_2. To expose the spinal cords, a ventral laminectomy was performed, and they were subsequently isolated together with the ventral roots and ganglia. Spinal cords were roughly (anterior–posterior length $\times$lateral width $\times$ ventral–dorsal height) $15 \times 1 \times 1.5$ mm, increasing with days postnatal.
Prior to live spinal cord transportation, the cord was placed in a sealed 50ml tube with 10ml aCSF previously bubbled with 95% O_2 and 5% CO_2. The air in the tube was flushed with 95% O_2 and 5% CO_2.
For fixed experiments, at the end of dissection the cords were fixed in 4% paraformaldehyde overnight at $4°C$. Fixative was then replaced with aCSF three times over the course of two days to remove any residual paraformaldehyde.
Triton X-100 (Sigma-Aldrich) nonionic surfactant was used to delipidate spinal cords. Samples (n=2) were studied during delpidation by replacing the aCSF media with aCSF media containing a specified % of Triton X during NMR recording. Samples (n=2) were also studied after delipidation with 10% Triton X in phosphate buffered saline (PBS) for two days, removal of Triton X by periodically replacing the PBS media for two more days, and equilibration in aCSF for a final day.

NMR hardware. NMR measurements were performed at 13.79 MHz proton frequency with a Kea2 spectrometer (Magritek, Wellington, New Zealand). A PM-10 NMR MOUSE (Magritek, Aachen, Germany) permanent magnet (42) provided a B_0 magnetic field, specially designed to be constant along an x-y (20 mm $\times$ 20 mm) plane parallel to the magnet's surface, but decreases rapidly and linearly in the perpendicular (y-direction) from the surface, providing a strong static magnetic field gradient (See Fig. 10(b)) (54). The NMR MOUSE was raised or lowered with a stepper motor with a step size of 50 μm in order to move $B_0 = 0.3239$ T, 13.79 MHz, to the precise depth within the sample (17 mm from the surface of the magnet). At this depth the magnetic field gradient $g = 15.3$ T/m, or 650 KHz/mm.

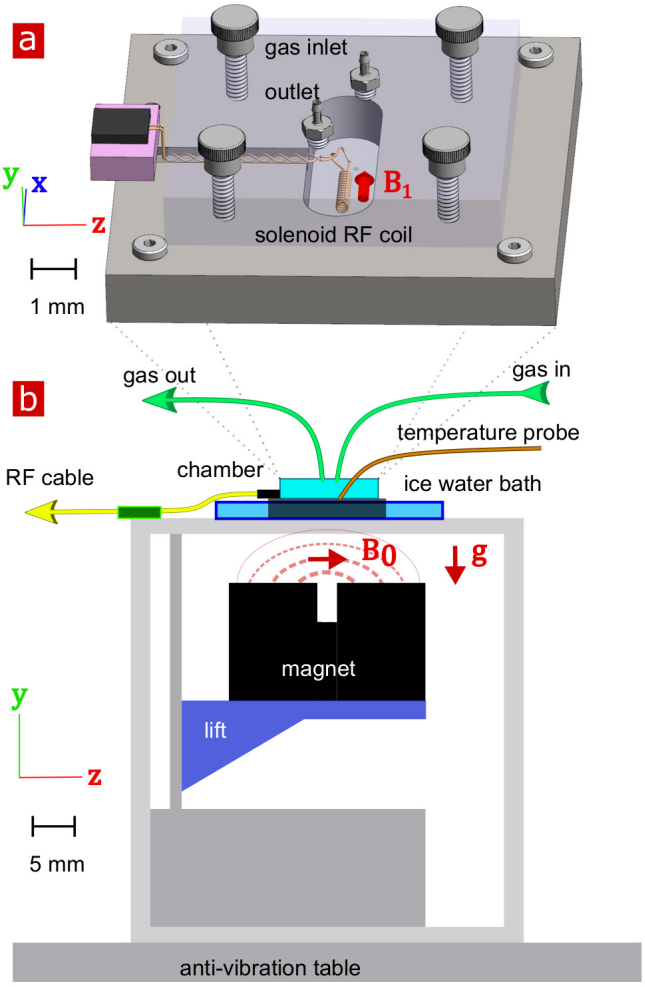

Fig. 10. Technical drawing of (b) experimental setup and (a) enlarged, 3-D view of the test chamber. The magnet (b) is drawn in the "service" position to show the field lines extending from one magnetic pole to the other. To perform measurements, the magnet would be raised such that the B_0 was correctly positioned relative to the sample. Vectors B_1, g and B_0 point in the x, y, and z directions respectively

Double-wrapped (length $\times$ inner diameter) 13×2 mm solenoid radiofrequency (RF) coils and an RF circuit were built in-house. The solenoid connected to the circuit board with detachable pin connectors. Tune and match used two trimmer capacitors with range 1–23 pF(NMAJ25HV, Knowles Voltronics). RF pulses were driven by a 100 W RF pulse amplifier (Tomco, Adelaide, Australia). (See SI and Fig. S5 for additional information and circuit design.)

NMR experimental methods. NMR measurements were performed in Prospa 3.22 (Magritek). All measurements set repetition time (TR) =2 s, $90°/180°$ pulse times =2 μs and amplitudes =-22/-16 dB, and acquired 2000 CPMG echoes

with 25 μs echo time. The acquisition time and dwell time were 4 and 0.5 μs respectively, leading to roughly a 400 μm slice thickness. The lift was positioned such that the signal was at a maximum, thus providing a slice through the center of the solenoid. Signal was phased such that the real signal was maximum and the mean of the imaginary signal was zero. Measurements were performed without regulating temperature ($22-26°$C) or else at a controlled temperature $25°$C when specified in figure captions.

Diffusion measurements were performed using the spin echo sequence (46) (Fig. S6(a)). τ was incremented linearly from 0.05 to 6.55 ms in 43 data points (corresponding to b values from 1.4 to 3,130,000 $\mathrm{s/mm^2}$) or, for live and some fixed specimen, from 0.05 to 3.3 ms in 22 points. (See SI for additional information.)

The DEXSY sequence (Fig. S6(b)) was written in-house and used eight phase cycle steps. For full 2-D DEXSY measurements (31), data points were acquired on a 21×21 b_1, b_2 grid by incrementing τ_1 linearly from 0.200 to 3.3 ms in an inner loop and τ_2 from 0.213 to 3.313 ms in an outer loop. For the rapid exchange measurement, points were acquired as a function of b_s and b_d by varying τ_1 and τ_2 accordingly. For rapid exchange measurements (38), the standard 4-point acquisition used one point at $b_s = 200$, $b_d = 20$ $\mathrm{s/mm^2}$, and three points along $b_s = 4500$ $\mathrm{s/mm^2}$ with $b_d = -4300$, -150, and $b_d = 4300$. Unless otherwise specified, the t_m list was [0.2, 4, 20, 160] ms for full DEXSYs and [0.2, 1, 2, 4, 7, 10, 20, 40, 80, 160, 300] ms for the rapid exchange measurement. (See SI and table S1 for sequence details and phase cycles.)

Standard CPMG T_2 (10 s TR, 8000 echoes) and saturation recovery T_1 (1 s TR, 21 recovery points logarithmically spaced to 10 s) measurements were performed, with all other parameters consistent with diffusion and exchange measurements. In all cases, data was monoexponential. (See Figs. S8 and S9.) The T_2/T_1 values were 275 ± 5/1870 ± 10 ms for aCSF (3 measurements), 155 ± 13/972 ± 53 ms for fixed spinal cords (n=10/4), and 176 ± 35/1030 ms for fixed spinal cords after delipidation (n=3/1).

NMR data analysis. 1-D distributions were fit using ℓ_2 regularization (48) and singular value decomposition (77, 78), with 50 grid points logarithmically spaced from 10^{-13} to 10^{-8} $\mathrm{m^2/s}$, and the regularization parameter chosen using the generalized cross validation (GCV) method (79). 2-D distributions were fit with an algorithm which uses ℓ_2 regularization and singular value decomposition, with 21x21 grid points logarithmically spaced from 10^{-13} to 10^{-8} $\mathrm{m^2/s}$ and the regularization parameter chosen by the L-curve method and held constant for all experiments. Exchanging fractions were calculated rapid measurement using Eqs. S8–S10 with $D_e = 10^{-9}$ and $D_i = 10^{-11}$ $\mathrm{m^2/s}$. AXRs from both full DEXSYs and the rapid exchange measurement were estimated from fits of a first order rate model Eq. S11–S12 (33, 38, 49), incorporating a non-zero initial condition to account for exchange during encoding (50). All analysis was performed using Matlab. (See SI for additional information.)

System characteristics led to high SNR diffusion measurements. Although SNR is highly dependent on the magnetic field strength, the decrease in SNR at low field is boosted by refocussing the signal 2000 times in a CPMG train for each data point (46). Moreover, the solenoid RF coil maximized the sample filling factor, boosting SNR roughly 10-fold from previous flat RF designs (80). RF pulses used little power, permitting short 2 μs RF pulse durations and producing negligible heat. The coil design allowed for short echo times which reduced relaxation during acquisition in the CPMG train, again boosting SNR. Significant attention was given to shielding and grounding the equipment to minimize noise pickup. All together, 1-D diffusion measurements obtained SNR > 600 (defined as the I_0/σ where σ is the standard deviation of the real channel measured at the noise floor).

Electrophysiological recording. Electrical activity from motoneurons was recorded with suction electrodes into which individual ventral roots (L6 or T10) were drawn after NMR measurements (n=4). The recorded signals were filtered (between 0.1 and 3 kHz) and amplified (gain: 1000), digitized at 10 kHz (Digidata 1500 B) and stored digitally on a computer. Episodes of data were analyzed off-line using Matlab. To elicit monosynaptic responses in motoneurons, the homonymous dorsal roots were stimulated with a single electrical pulse (250 μs duration) repeated 5 times at 30 s intervals. The threshold for a given spinal root was defined as the lowest current intensity at which that root had to be stimulated to elicit a monosynaptic response in 5/5 attempts. Recordings were obtained at 5 $\times$ threshold.

ACKNOWLEDGEMENTS
We thank Randall Pursley, Danny Trang, and Marcial Garmendia-Cedillos for electrical engineering help, Sarah Avram for Triton X delipidation protocol advice, Alexandru Avram for general suggestions, Uzi Eliav for phase cycling expertise, and Elizabeth Murphy for resource provisions. Special thanks to Velencia Witherspoon for suggesting the solenoid coil and the D_2O wash. NHW, DB and PJB were all supported by the IRP of the NICHD, NIH. DB was also supported by the Center for Neuroscience and Regenerative Medicine, Henry Jackson Foundation, Bethesda, MD.

Bibliography

1. Peter J Basser, James Mattiello, and Denis LeBihan. Mr diffusion tensor spectroscopy and imaging. *Biophysical journal*, 66(1):259–267, 1994.
2. Christian Beaulieu and Peter S Allen. Water diffusion in the giant axon of the squid: implications for diffusion-weighted mri of the nervous system. *Magnetic Resonance in Medicine*, 32(5):579–583, 1994.
3. Christian Beaulieu. The basis of anisotropic water diffusion in the nervous system–a technical review. *NMR in Biomedicine*, 15(7-8):435–455, 2002.
4. Kwanghun Chung, Jenelle Wallace, Sung-Yon Kim, Sandhiya Kalyanasundaram, Aaron S Andalman, Thomas J Davidson, Julie J Mirzabekov, Kelly A Zalocusky, Joanna Mattis, Aleksandra K Denisin, et al. Structural and molecular interrogation of intact biological systems. *Nature*, 497(7449):332, 2013.
5. Kazuki Tainaka, Tatsuya C Murakami, Etsuo A Susaki, Chika Shimizu, Rie Saito, Kei Takahashi, Akiko Hayashi-Takagi, Hiroshi Sekiya, Yasunobu Arima, Satoshi Nojima, et al. Chemical landscape for tissue clearing based on hydrophilic reagents. *Cell reports*, 24(8):2196–2210, 2018.
6. Christoph Leuze, Markus Aswendt, Emily Ferenczi, Corey W Liu, Brian Hsueh, Maged Goubran, Qiyuan Tian, Gary Steinberg, Michael M Zeineh, Karl Deisseroth, et al. The separate effects of lipids and proteins on brain mri contrast revealed through tissue clearing. *Neuroimage*, 156:412–422, 2017.
7. Paul T Callaghan, Christoph H Arns, Petrik Galvosas, Mark W Hunter, Ying Qiao, and Kate E Washburn. Recent fourier and laplace perspectives for multidimensional nmr in porous media. *Magnetic resonance imaging*, 25(4):441–444, 2007.
8. Erwin L Hahn. Spin echoes. *Physical review*, 80(4):580, 1950.
9. Herman Y Carr and Edward M Purcell. Effects of diffusion on free precession in nuclear magnetic resonance experiments. *Physical review*, 94(3):630, 1954.

10. Paul T Callaghan, Andrew Coy, David MacGowan, Ken J Packer, and Fernando O Zelaya. Diffraction-like effects in nmr diffusion studies of fluids in porous solids. *Nature*, 351(6326): 467, 1991.
11. P.T. Callaghan. *Translational Dynamics and Magnetic Resonance Principles of Pulsed Gradient Spin Echo NMR*. Oxford University Press, 2011.
12. Edward O Stejskal and John E Tanner. Spin diffusion measurements: spin echoes in the presence of a time-dependent field gradient. *The journal of chemical physics*, 42(1):288–292, 1965.
13. Donald E Woessner. Effects of diffusion in nuclear magnetic resonance spin-echo experiments. *The Journal of Chemical Physics*, 34(6):2057–2061, 1961.
14. Richard Conable Wayne and Robert M Cotts. Nuclear-magnetic-resonance study of self-diffusion in a bounded medium. *Physical Review*, 151(1):264, 1966.
15. Baldwin Robertson. Spin-echo decay of spins diffusing in a bounded region. *Physical Review*, 151(1):273, 1966.
16. CH Neuman. Spin echo of spins diffusing in a bounded medium. *The Journal of Chemical Physics*, 60(11):4508–4511, 1974.
17. Thomas M de Swiet and Pabitra N Sen. Decay of nuclear magnetization by bounded diffusion in a constant field gradient. *The Journal of chemical physics*, 100(8):5597–5604, 1994.
18. MD Hurlimann, KG Helmer, TM Deswiet, and PN Sen. Spin echoes in a constant gradient and in the presence of simple restriction. *Journal of Magnetic Resonance*, 113:260–264, 1995.
19. Dan Benjamini and Peter J Basser. Magnetic resonance microdynamic imaging reveals distinct tissue microenvironments. *NeuroImage*, 163:183–196, 2017.
20. D Le Bihan, C T Moonen, P C van Zijl, J Pekar, and D DesPres. Measuring random microscopic motion of water in tissues with MR imaging: a cat brain study. *Journal of Computer Assisted Tomography*, 15(1):19–25, 1991.
21. Thoralf Niendorf, Rick M. Dijkhuizen, David G. Norris, Menno van Lookeren Campagne, and Klaas Nicolay. Biexponential diffusion attenuation in various states of brain tissue: Implications for diffusion-weighted imaging. *Magnetic Resonance in Medicine*, 36(6):847–57, 1996.
22. R V Mulkern, H P Zengingonul, R L Robertson, P Bogner, K H Zou, H Gudbjartsson, C R Guttmann, D Holtzman, W Kyriakos, F A Jolesz, and S E Maier. Multi-component apparent diffusion coefficients in human brain: relationship to spin-lattice relaxation. *Magnetic Resonance in Medicine*, 44(2):292–300, 2000.
23. Josef Pfeuffer, Stephen W Provencher, and Rolf Gruetter. Water diffusion in rat brain in vivo as detected at very largeb values is multicompartmental. *Magnetic Resonance Materials in Physics, Biology and Medicine*, 8(2):98–108, 1999.
24. Ileana O Jelescu, Jelle Veraart, Els Fieremans, and Dmitry S Novikov. Degeneracy in model parameter estimation for multi-compartmental diffusion in neuronal tissue. *NMR in Biomedicine*, 29(1):33–47, 2016.
25. Itamar Ronen, Steen Moeller, Kamil Ugurbil, and Dae-Shik Kim. Analysis of the distribution of diffusion coefficients in cat brain at 9.4 T using the inverse Laplace transformation. *Magnetic Resonance Imaging*, 24(1):61–68, 2006.
26. Dan Benjamini and Peter J. Basser. Water mobility spectral imaging of the spinal cord: Parametrization of model-free Laplace MRI. *Magnetic Resonance Imaging*, 56:187–193, 2019.
27. Jan Andrasko. Water diffusion permeability of human erythrocytes studied by a pulsed gradient nmr technique. *Biochimica et Biophysica Acta (BBA)-General Subjects*, 428(2): 304–311, 1976.
28. A Reginald Waldeck, M Hossein Nouri-Sorkhabi, David R Sullivan, and Philip W Kuchel. Effects of cholesterol on transmembrane water diffusion in human erythrocytes measured using pulsed field gradient nmr. *Biophysical chemistry*, 55(3):197–208, 1995.
29. Josef Pfeuffer, Ulrich Flögel, Wolfgang Dreher, and Dieter Leibfritz. Restricted diffusion and exchange of intracellular water: theoretical modelling and diffusion time dependence of 1h nmr measurements on perfused glial cells. *NMR in Biomedicine: An International Journal Devoted to the Development and Application of Magnetic Resonance In Vivo*, 11(1):19–31, 1998.
30. Peter E Thelwall, Samuel C Grant, Greg J Stanisz, and Stephen J Blackband. Human erythrocyte ghosts: exploring the origins of multiexponential water diffusion in a model biological tissue with magnetic resonance. *Magnetic Resonance in Medicine: An Official Journal of the International Society for Magnetic Resonance in Medicine*, 48(4):649–657, 2002.
31. P. T. Callaghan and I. Furó. Diffusion-diffusion correlation and exchange as a signature for local order and dynamics. *The Journal of Chemical Physics*, 120(8):4032–4038, 2004.
32. Diana Bernin and Daniel Topgaard. NMR diffusion and relaxation correlation methods: New insights in heterogeneous materials. *Current Opinion in Colloid and Interface Science*, 18 (3):166–172, 2013. ISSN 1359-0294.
33. Dan Benjamini, Michal E. Komlosh, and Peter J. Basser. Imaging local diffusive dynamics using diffusion exchange spectroscopy MRI. *Physical Review Letters*, 118:158003, Apr 2017.
34. Ruiliang Bai, Dan Benjamini, Jian Cheng, and Peter J Basser. Fast, accurate 2d-mr relaxation exchange spectroscopy (rexsy): Beyond compressed sensing. *The Journal of chemical physics*, 145(15):154202, 2016.
35. Dan Benjamini and Peter J. Basser. Use of marginal distributions constrained optimization (MADCO) for accelerated 2D MRI relaxometry and diffusometry. *Journal of Magnetic Resonance*, 271:40–45, 2016. ISSN 1090-7807.
36. Dan Benjamini and Peter J. Basser. Towards clinically feasible relaxation-diffusion correlation MRI using MADCO. *Microporous and Mesoporous Materials*, 269:93–96, 2018.
37. Ingrid Åslund, Agnieszka Nowacka, Markus Nilsson, and Daniel Topgaard. Filter-exchange PGSE NMR determination of cell membrane permeability. *Journal of Magnetic Resonance*, 200(2):291 – 295, 2009. ISSN 1090-7807.
38. Teddy X Cai, Dan Benjamini, Michal E Komlosh, Peter J Basser, and Nathan H Williamson. Rapid detection of the presence of diffusion exchange. *Journal of Magnetic Resonance*, 297:17–22, 2018.
39. Markus Nilsson, Samo Lasič, Ivana Drobnjak, Daniel Topgaard, and Carl-Fredrik Westin. Resolution limit of cylinder diameter estimation by diffusion mri: The impact of gradient waveform and orientation dispersion. *NMR in Biomedicine*, 30(7):e3711, 2017.
40. William S Price. Pulsed-field gradient nuclear magnetic resonance as a tool for studying translational diffusion: Part ii. experimental aspects. *Concepts in Magnetic Resonance: An Educational Journal*, 10(4):197–237, 1998.
41. R Kimmich, W Unrath, G Schnur, and E Rommel. Nmr measurement of small self-diffusion coefficients in the fringe field of superconducting magnets. *Journal of Magnetic Resonance*, 91(1):136–140, 1991.
42. G Eidmann, R Savelsberg, Peter Blümler, and Bernhard Blümich. The nmr mouse, a mobile universal surface explorer. *Journal of Magnetic Resonance*, 122:104–109, 1996.
43. KJ Carlton, MR Halse, and John H Strange. Diffusion-weighted imaging of bacteria colonies in the strafi plane. *Journal of Magnetic Resonance*, 143(1):24–29, 2000.
44. K Potter, RL Kleinberg, FJ Brockman, and EW McFarland. Assay for bacteria in porous media by diffusion-weighted nmr. *Journal of Magnetic Resonance, Series B*, 113(1):9–15, 1996.
45. Janez Stepišnik, Carlos Mattea, Siegfried Stapf, and Aleš Mohorič. Molecular velocity autocorrelation of simple liquids observed by nmr mgse method. *The European Physical Journal B*, 91(11):293, 2018.
46. D.G. Rata, F. Casanova, J. Perlo, D.E. Demco, and B. Blümich. Self-diffusion measurements by a mobile single-sided nmr sensor with improved magnetic field gradient. *Journal of Magnetic Resonance*, 180(2):229 – 235, 2006. ISSN 1090-7807. doi: https://doi.org/10.1016/j.jmr.2006.02.015.
47. Oliver Neudert, Siegfried Stapf, and Carlos Mattea. Diffusion exchange nmr spectroscopy in inhomogeneous magnetic fields. *Journal of Magnetic Resonance*, 208(2):256–261, 2011.
48. Stephen W. Provencher. A constrained regularization method for inverting data represented by linear algebraic or integral equations. *Computer Physics Communications*, 27(3):213–227, 1982.
49. K. E. Washburn and P. T. Callaghan. Tracking pore to pore exchange using relaxation exchange spectroscopy. *Physical Review Letters*, 97:175502, Oct 2006.
50. Nathan H Williamson, April M Dower, Sarah L Codd, Amber L Broadbent, Dieter Gross, and Joseph D Seymour. Glass dynamics and domain size in a solvent-polymer weak gel measured by multidimensional magnetic resonance relaxometry and diffusometry. *Physical review letters*, 122(6):068001, 2019.
51. Maxime Van Landeghem, Agnes Haber, Jean-Baptiste D'espinose De Lacaillerie, and Bernhard Blümich. Analysis of multisite 2d relaxation exchange nmr. *Concepts in Magnetic Resonance Part A*, 36(3):153–169, 2010.
52. CLG Ham, JML Engels, GT Van de Wiel, and A Machielsen. Peripheral nerve stimulation during mri: effects of high gradient amplitudes and switching rates. *Journal of Magnetic Resonance Imaging*, 7(5):933–937, 1997.
53. M Köpf, C Corinth, O Haferkamp, and TF Nonnenmacher. Anomalous diffusion of water in biological tissues. *Biophysical journal*, 70(6):2950–2958, 1996.
54. J Perlo, F Casanova, and B Blümich. Profiles with microscopic resolution by single-sided nmr. *Journal of magnetic resonance*, 176(1):64–70, 2005.
55. Federico Casanova, Juan Perlo, and Bernhard Blümich. *Single-sided NMR*. Springer, 2011.
56. Ernesto Danieli and Bernhard Blümich. Single-sided magnetic resonance profiling in biological and materials science. *Journal of Magnetic Resonance*, 229:142–154, 2013.
57. Christian Rehorn and Bernhard Blümich. Cultural heritage studies with mobile nmr. *Angewandte Chemie International Edition*, 57(25):7304–7312, 2018.
58. J Mitchell, TC Chandrasekera, and LF Gladden. Numerical estimation of relaxation and diffusion distributions in two dimensions. *Progress in nuclear magnetic resonance spectroscopy*, 62:34–50, 2012.
59. David L Buckley, Jonathan D Bui, M Ian Phillips, Tibor Zelles, Benjamin A Inglis, H Daniel Plant, and Stephen J Blackband. The effect of ouabain on water diffusion in the rat hippocampal slice measured by high resolution nmr imaging. *Magnetic Resonance in Medicine: An Official Journal of the International Society for Magnetic Resonance in Medicine*, 41(1):137–142, 1999.
60. JD Bui, DL Buckley, MI Phillips, and SJ Blackband. Nuclear magnetic resonance imaging measurements of water diffusion in the perfused hippocampal slice during n-methyl-d-aspartate-induced excitotoxicity. *Neuroscience*, 93(2):487–490, 1999.
61. Timothy M Shepherd, Stephen J Blackband, and Edward D Wirth III. Simultaneous diffusion mri measurements from multiple perfused rat hippocampal slices. *Magnetic Resonance in Medicine: An Official Journal of the International Society for Magnetic Resonance in Medicine*, 48(3):565–569, 2002.
62. Timothy M Shepherd, Peter E Thelwall, Greg J Stanisz, and Stephen J Blackband. Aldehyde fixative solutions alter the water relaxation and diffusion properties of nervous tissue. *Magnetic Resonance in Medicine: An Official Journal of the International Society for Magnetic Resonance in Medicine*, 62(1):26–34, 2009.
63. Nitzan Tirosh and Uri Nevo. Neuronal activity significantly reduces water displacement: Dwi of a vital rat spinal cord with no hemodynamic effect. *Neuroimage*, 76:98–107, 2013.
64. Ruiliang Bai, Craig V Stewart, Dietmar Plenz, and Peter J Basser. Assessing the sensitivity of diffusion mri to detect neuronal activity directly. *Proceedings of the National Academy of Sciences*, 113(12):E1728–E1737, 2016.
65. Sarah E Mailhiot, Nathan H Williamson, Jennifer R Brown, Joseph D Seymour, Sarah L Codd, and Ronald K June. $t_1 - t_2$ correlation and biopolymer diffusion within human osteoarthritic cartilage measured with nuclear magnetic resonance. *Applied Magnetic Resonance*, 48(4):407–422, 2017.
66. L Masaro and XX Zhu. Physical models of diffusion for polymer solutions, gels and solids. *Progress in polymer science*, 24(5):731–775, 1999.
67. Lawrence L Latour, Karel Svoboda, Partha P Mitra, and Christopher H Sotak. Time-dependent diffusion of water in a biological model system. *Proceedings of the National Academy of Sciences*, 91(4):1229–1233, 1994.
68. Dmitry S Novikov, Jens H Jensen, Joseph A Helpern, and Els Fieremans. Revealing mesoscopic structural universality with diffusion. *Proceedings of the National Academy of Sciences*, 111(14):5088–5093, 2014.
69. Eric R Kandel, James H Schwartz, Thomas M Jessell, Department of Biochemistry, Molecular Biophysics Thomas Jessell, Steven Siegelbaum, and AJ Hudspeth. *Principles of neural*

science, volume 5. McGraw-hill New York, 2013.

70. Dan Benjamini, Jonathan J. Elsner, Meital Zilberman, and Uri Nevo. Pore size distribution of bioresorbable films using a 3-D diffusion NMR method. *Acta Biomaterialia*, 10:2762–2768, 2014.
71. Dan Benjamini, Michal E. Komlosh, Lynne A. Holtzclaw, Uri Nevo, and Peter J. Basser. White matter microstructure from nonparametric axon diameter distribution mapping. *NeuroImage*, 135:333 – 344, 2016. ISSN 1053-8119.
72. James D Quirk, G Larry Bretthorst, Timothy Q Duong, Avi Z Snyder, Charles S Springer Jr, Joseph JH Ackerman, and Jeffrey J Neil. Equilibrium water exchange between the intra- and extracellular spaces of mammalian brain. *Magnetic Resonance in Medicine: An Official Journal of the International Society for Magnetic Resonance in Medicine*, 50(3):493–499, 2003.
73. Markus Nilsson, Jimmy Lätt, Danielle van Westen, Sara Brockstedt, Samo Lasič, Freddy Ståhlberg, and Daniel Topgaard. Noninvasive mapping of water diffusional exchange in the human brain using filter-exchange imaging. *Magnetic Resonance in Medicine*, 69(6): 1572–1580, 2013.
74. Ruiliang Bai, Charles S Springer Jr, Dietmar Plenz, and Peter J Basser. Fast, na+/k+ pump driven, steady-state transcytolemmal water exchange in neuronal tissue: A study of rat brain cortical cultures. *Magnetic Resonance in Medicine*, 79(6):3207–3217, 2018.
75. Ruiliang Bai, Charles S Springer Jr, Dietmar Plenz, and Peter J Basser. Brain active transmembrane water cycling measured by mr is associated with neuronal activity. *Magnetic resonance in medicine*, 81(2):1280–1295, 2019.
76. Philip W Kuchel and Gheorghe Benga. Why does the mammalian red blood cell have aquaporins? *Biosystems*, 82(2):189–196, 2005.
77. L. Venkataramanan, Yi-Qiao Song, and Martin D. Hürlimann. Solving Fredholm integrals of the first kind with tensor product structure in 2 and 2.5 dimensions. *IEEE Trans. Signal. Process.*, 50(5):1017–1026, 2002. ISSN 1053-587X.
78. S Godefroy and PT Callaghan. 2d relaxation/diffusion correlations in porous media. *Magnetic Resonance Imaging*, 21(3-4):381–383, 2003.
79. Gene H. Golub, Michael Heath, and Grace Wahba. Generalized Cross-Validation as a Method for Choosing a Good Ridge Parameter. *Technometrics*, 21(2):215, 1979.
80. Ruiliang Bai, Andreas Klaus, Tim Bellay, Craig Stewart, Sinisa Pajevic, Uri Nevo, Hellmut Merkle, Dietmar Plenz, and Peter J Basser. Simultaneous calcium fluorescence imaging and mr of ex vivo organotypic cortical cultures: a new test bed for functional mri. *NMR in Biomedicine*, 28(12):1726–1738, 2015.

Theory

Diffusion signal attenuation models. Attenuation of the MR signal in a spin echo diffusion experiment under a static magnetic field gradient can exhibit three diffusion regimes corresponding to three different characteristic length scales: the restriction length l_s, the diffusion length, $l_d = \sqrt{D_0\tau}$, and the dephasing length, $l_g = (D_0/\gamma g)^{1/3}$ where $D_0 = 2.15\ \mathrm{m}^2/\mathrm{s}$ is the diffusion coefficient of free water, τ is the time between the first 90° and the 180° radio frequency refocussing pulses of the spin echo sequence or $1/2$ the echo time TE, and γ is the gyromagnetic ratio (1). The diffusion length is the average distance that water diffuses during the time τ. In the spin echo diffusion measurements, τ was linearly increased from 0.05 to 3.3 or to 6.6 ms, corresponding to $l_D = 0.33$, 2.7, and 3.7 μm respectively. The dephasing length is the distance that spins must displace in order to dephase by 2π radians. For the 15.3 $\mathrm{T/m}$ gradient used here, $l_g = 800\ \mathrm{nm}$. The shortest of these three length scales determines the regime that applies to the diffusing spins, and thus dictates the asymptotic behavior of the spin echo decay.

Free diffusion regime. The free diffusion regime occurs when l_D is the shortest characteristic length scale. This regime was first described by Hahn (2) and then the diffusion coefficient of water was measured by Carr and Purcell (3), both using static magnetic field gradients. In this regime, the signal decays by (4)

$$\begin{aligned} I(\tau)/I_0 &= \exp\left(-\frac{2}{3}D_0\gamma^2 g^2\tau^3\right) \\ &= \exp\left(-\frac{2}{3}\left(\frac{l_D}{l_g}\right)^6\right) \\ &= \exp(-bD_0). \end{aligned} \tag{S1}$$

Water diffusion is often modeled as Gaussian with an effective or apparent diffusion coefficient D, rather than D_0, and in the limit of low attenuation $D = \langle D\rangle$. "Apparent" implies that the measured diffusion coefficient will depend on the experimental parameters (5). This is particularly true when using Eq. S1 to model signal which includes water in other regimes. The use of b coefficient or factor comes from diffusion MRI literature (6).

Localization regime. The localization regime occurs when l_s is the shortest characteristic length scale. In this regime, signal near the restrictive surfaces will dephase more slowly than signal farther away. While the entire decay curve can be quite complicated in the long-time (τ) limit the signal was experimentally characterized by Hurlimann et al. (1) and theoretically modeled by de Swiet et al (7), and shown to attenuate as

$$\begin{aligned} I(\tau)/I_0 &= c\frac{D_0^{1/3}}{\gamma^{1/3}g^{1/3}l_s}\exp\left(-a_1 D_0^{1/3}\gamma^{2/3}g^{2/3}\tau\right) \\ &= c\frac{l_g}{l_s}\exp\left(-a_1\left(\frac{l_D}{l_g}\right)^2\right), \end{aligned} \tag{S2}$$

where $a_1 = 1.0188$. The prefactor c varies depending on the geometry and equals 5.8841 for water restricted between parallel plates (7). Note that l_s affects the fraction of signal present in the asymptotic limit but does not affect the decay. By varying τ under a static gradient, we see that the signal attenuates exponentially with τ, $(l_D/l_g)^2$ or $(bD_0)^{1/3}$.

Motional averaging regime. The motional averaging regime occurs when l_g is the shortest characteristic length scale. Signal attenuates very slowly and water can diffuse across the restricted volume many times before dephasing appreciably. Signal decay in the motional averaging regime was first experimentally measured by Wayne and Cotts (8) and subsequently modeled by Robertson (9). Neuman derived the signal attenuation models for water restricted between parallel plates and within cylinders oriented perpendicular to g, and within spheres (10). We focus on the model for spheres of radius R for which the signal attenuates by

$$I(\tau)/I_0 = \exp\left(-\frac{2\gamma^2 g^2}{D_0}\sum_{m=1}^{\infty}\frac{\alpha_m^{-4}}{\alpha_m^2R^2-2}\left(2\tau - \frac{3-4\exp(-\alpha_m^2D_0\tau)+\exp(-\alpha_m^2D_0\,2\tau)}{\alpha_m^2D_0}\right)\right) \tag{S3}$$

where α_m is the mth root of

$$\alpha_m R J'_{3/2}(\alpha_m R) - \frac{1}{2}J_{3/2}(\alpha_m R) = 0 \tag{S4}$$

for which the first 5 roots are $\alpha_m R = 2.0815$, 5.940, 9.206, 12.405, and 15.579. In the limit of long τ relative to the timescale to diffuse across the restriction, Eq. S3 becomes

$$\begin{aligned} I(\tau)/I_0 &= \exp\left(-\frac{8}{175}\frac{R^4\gamma^2 g^2}{D_0}\left(2\tau - \frac{581}{840}\frac{R^2}{D}\right)\right) \\ &\approx \exp\left(-\frac{4}{175}\left(\frac{l_D}{l_g}\right)^2\left(\frac{l_s}{l_g}\right)^4\right). \end{aligned} \tag{S5}$$

In the long-time limit, decay models for other geometries vary from Eq. S5 by a scaling within the exponential.
As in the long-time limit of the localization regime, decay of signal in the motional averaging regime is exponential with τ, $(l_D/l_g)^2$ or $(bD_0)^{1/3}$. Exchange also occurs on the timescale of τ and can be incorporated into the decay model by multiplying by $\exp(-2\tau\mathrm{AXR})$ where AXR is the apparent exchange rate(11).
The decay is due to the random motion of the center-of-mass of the spins within the volume rather than spins diffusing across the whole length of the restricted pore, hence the term "motional averaging". The effect is the extreme case of when δ approaches Δ in pulsed gradient measurements, which researchers have commented leads to restrictions appearing smaller than they actually are (12–14). Given the gradient strength limitations on human MRI scanners, the clinical translation of advanced diffusion MRI methods requires the use of gradient pulses with maximum amplitude for efficient diffusion encoding (15). Consequently, clinical implementations of many advanced diffusion MRI preparations can be adjusted to effectively resemble/be equivalent to experiments in a static gradient field.
Decay models for the various regimes are compared in Fig. 6 of the main manuscript.

Supplementary results

Penetration timescales. The methods were used to follow penetration of deuterated water D_2O into the tissue as well as the delipidation of the tissue via Triton X. For the D_2O wash (Fig. S2), I_0 decreased to 0.36 two minutes after washing, indicating that water in the tissue communicates with the aCSF on timescales of minutes. Exchange and restricted fractions decreased during delipidation on the timescale of roughly one day (Fig. S3). Mass transport theory estimates the timescale to equilibrate a concentration gradient across the tissue as ≈ 1 min for water and ≈ 3 hrs for Triton X based on $t = r^2/4D$ (16) with specimen radius $r = 0.7$ mm and measured $D = 2.15\times10^{-9}\ \mathrm{m^2/s}$ for water and $D = 1.3\times10^{-11}\ \mathrm{m^2/s}$ for Triton X (see supplementary Fig. S4). The timescale of water penetration was consistent with mass transport theory (16), but the timescale of Triton X penetration and delipidation was longer than predicted. An increased time is expected due to the reaction front which develops as Triton X delipidates, slowing its overall penetration.

Testing the rapid exchange measurement on fixed spinal chord tissue. Given that this is the first time the rapid exchange measurement has been used with a static gradient as well as on anything other than an ideal phantom, a full characterization of the signal seemed necessary. Details of the rapid exchange measurement method can be found in Cai, et al., 2018 (17), and the supplementary methods section (below). In this section we test the behavior of the signal acquired as a function of b_d, b_s, and t_m on fixed spinal cord and compare results to the predicted exchange behavior (17).
The curvature along slices of $b_s = 4500\ \mathrm{s/mm^2}$ as a function of b_d at different mixing times is shown in Fig. S9. The signal is concave up with maximum at $b_d = \pm4500$, minimum at $b_d = 0$, and roughly symmetric about $b_d = 0$, as expected. Exchange increases with mixing time, also as expected. From this, we can conclude that the 4-point method (discussed below) can capture the exchange with maximal sensitivity.
The optimal b_s maximizes the finite difference (Eq. S8) and provides optimal sensitivity to exchange in the presence of noise. However, different b_s values may diffusion-weight the measurement towards exchange between different pools. Fig. S10 shows that the finite difference reaches a maximum near $b_s = 6000\ \mathrm{s/mm^2}$. The value $b_d = 4500\ \mathrm{s/mm^2}$ used in this study is thus near the optimum. Additionally, from this data it was found that the exchange rate is not significantly different between b_s values, indicating that AXR is not very sensitive to b_s.
The four-point method allowed for high temporal resolution of exchange. Fig. S11 shows a dense sampling of f as a function of t_m, acquired overnight on a fixed spinal cord specimen. The data shows the $t_m = 0.1$ ms point to be not well behaved, with f decreasing from $t_m = 0.1$ to $0.2ms$, but increases from $t_m = 0.2$ ms onwards, indicating that $t_m = 0.2$ is a good point for the minimum t_m. The exchange plateaus near $t_m = 100$ ms and stays roughly constant to $t_m = 300$ ms, indicating that $t_m = 300$ ms is a good point for the maximum t_m because it captures the maximum, steady state exchange, as well as does not show T_1 relaxation effects (in particular due to differences in T_1 between exchanging pools (17)). The data was fit with the first-order rate model, Eq. S12, and the value (presented in the figure caption) was not statistically different from the less-dense sampling used throughout the paper. The dense sampling shows that the data is not fully explained by the first order rate model; it rises up quicker and plateaus slower. However, rather than fitting a model with more parameters, e.g. a model with two AXRs, we choose to stick to the first order rate model with one AXR. The dense sampling also re-iterates $f(t_m = 0) \neq 0$, thus calling for a non-zero initial condition (discussed below).

Supplementary Materials and Methods

Test chamber. The bottom portion of the experimental test chamber was made of aluminum to provide good heat conduction to the media. A bored-out rectangular hole with a glass cover slide glued to the bottom held the media, solenoid, and spinal cord. Aluminum parts that contacted aCSF were coated with a thin layer of RTV silicone to avoid corrosion. The top of the chamber was made from poly(methyl methacrylate) (PMMA) with two inlets for inflow and outflow of the gas and a hole for the PicoM fiber optic temperature sensor (Opsens Solutions Inc., Québec, Canada). Temperature measurements were not affected by RF and did not induce noise in the RF system. The temperature of the bath was monitored and recorded continuously. The top slide was secured and mounted to the bottom part with four screws. The NMR solenoid coil was glued to the glass cover slip bottom with a hot glue gun. Two separate chambers and solenoid coils were built for live and fixed spinal cord specimen.

NMR hardware. The solenoid radiofrequency (RF) coils and the circuit were built in-house. Solenoids were made from wrapping two concentric layers of AWG 30 copper wire around a #2-56 plastic screw totaling 39 turns resulting in 2 mm inner diameter 4 mm outer diameter, 1.3 cm length. The resulting coils had an inductance L $\sim$ 600 nH and impedance X $\sim$ 52 Ω at 13.79 MHz.

The solenoid connected to a circuit board with detachable pin connectors. (The circuit design is shown in Fig. S5.) The circuit used two trimmer capacitors (NMAJ25HV, Knowles Voltronics) with tunable range 1–23 pF for tune and match. The circuit board was connected to the Kea2 spectrometer by a 50 Ω coax cable. The coil matched to -34 dB at 13.79 MHz when immersed in aCSF. RF pulses were driven by a 100 W RF pulse amplifier (Tomco, Adelaide, Australia).

1-D spin echo diffusion. A standard pulse sequence (SEdec in Prospa) was used for measuring diffusion with a static gradient (18) built off of a spin echo followed by a Carr–Purcell–Meiboom–Gill (CPMG) echo train (2, 3, 19), as shown in Fig. S6a. The phase cycle list was four scans long (20).

Signal from the CPMG train is summed up as one data point. This summation provides a significant boost in the signal-to-noise ratio (SNR). Only signal from the real channel (rather than signal magnitude) is taken. This leads to zero-mean Gaussian rather than Rician noise, a significant benefit for multiexponential signal analysis. The echo time of the spin echo τ is incremented in successive loops of the experiment to encode for diffusion. For water and with large gradient the attenuation due to T_2 relaxation during τ is insignificant. Signal can be modeled using Eq. S1 for pure liquids such as water. In heterogeneous materials such as biological tissue, water in different parts of the material experience different hindrances and restrictions. Each sub-ensemble of water molecules has its own effective self-diffusion coefficients. The signal can be modeled as arising from the distribution of effective or apparent self-diffusion coefficients of the water in the different environments using

$$I(b)/I_0 = \int_0^\infty P(D)e^{-bD}dD. \tag{S6}$$

Static gradient DEXSY sequence and phase cycles. Attention was paid to phase cycles for the static gradient DEXSY sequence (Figure S6) due to each RF pulse being imperfect and exciting multiple coherence pathways when the inhomogeneity of the magnetic field is greater than the bandwidth of the RF pulses (21). The phase cycle list was eight scans long, shown in Table S1.

Although the phase cycle list is not exhaustive, we found the signal to be well-behaved on a non-exchanging two-pool system comprised of a capillary filled with polydymethylsyloxane bathed in water. Signal as a function of b_1 or b_2 were symmetric and decayed the same as signal as a function of b from the 1-D SEdec sequence. Additionally, signal was flat along slices of constant b_s and the 2-D DEXSY map showed two diffusion coefficients along the $D_1 = D_2$ diagonal equal to D_{water} and D_{PDMS}. One exception was that the phase cycles let through signals which do not form a gradient echo when they see the storage pulse, but do form a gradient echo upon acquisition, thus seeing the sequence as a 1-D stimulated echo diffusion. This became apparent due to additional refocussing when $b_1 = b_2$. This was found to be an issue with a previous miniature flat RF coil design (22) but went away when switching to the solenoid RF coil, thus it is likely an issue of B_1 inhomogeneity of the miniature flat RF coil (23). To avoid refocussing this signal, points were never acquired exactly on $b_1 = b_2$. Also note that the static gradient acts as a crusher during the storage interval. The sequence selects both compensated and uncompensated signals (24). The sequence can be compared and contrasted to another DEXSY sequence developed for static gradients but using stimulated echoes for diffusion encoding (25)

Fig. S6b shows the static gradient spin echo DEXSY sequence. In this sequence, molecules are encoded for their diffusion coefficient in their local environment during the first interval τ_1. Magnetization is then stored for a mixing time, t_m during which time molecules move freely and may exchange between diffusive environments. (Note that this definition of t_m is like the definition used for T_2–T_2 (26), and is different from the original definition presented by Callaghan and Furó which included the gradient pulse duration (27). We choose not to use that definition since τ is changing in a DEXSY measurement where t_m is meant to be held constant.) Molecules are again encoded for diffusion during τ_2 and then signal is acquired in a CPMG train.

Full DEXSY. The classic way to analyze the full 2-D DEXSY is as a diffusion exchange distribution, related to the signal through

$$I(b_1,b_2) = \int_0^\infty \int_0^\infty P(D_1,D_2)e^{-b_1D_1-b_2D_2}dD_1dD_2, \tag{S7}$$

a 2-D version of Eq. S6. The diffusion encoding variables, b_1 and b_2 are varied by independently varying τ_1 and τ_2. Molecules which do not exchange between environments will have the same diffusion coefficient during τ_1 and τ_2 contributing to populations on the diagonal of the 2-D distribution (see, e.g., Fig. 2a and b in (17)). Molecules which do exchange and thus are encoded with different diffusion coefficients between the two τ will contribute to off-diagonal exchange peaks in the 2-D distribution.

Rapid exchange measurement. Alternatively to the full DEXSY, we recently introduced a rapid method for measuring exchanging fractions which relied on curvature of the raw signal after a variable transformation (28). In particular, this method shows that exchange between diffusion environments results in the raw data being curved up along a slice of constant $b_s = b_1 + b_2$ (see Fig. 2c and d in (17)). The exchanging fraction scales with $(\partial^2 I/\partial b_d^2)$ where $bd = b_2 - b_1$. The second derivative can be approximated with the 2nd order finite difference method,

$$\frac{\partial^2 I}{\partial b_d^2}\Big|_{b_d=b} \approx \frac{I\Big|_{b_d=b-\Delta b_d} - 2I\Big|_{b_d=b} + I\Big|_{b_d=b+\Delta b_d}}{\Delta b_d^2}, \tag{S8}$$

omitting higher order terms. The greatest sensitivity to exchange is when the central point is acquired at $b_d = 0$ and the edges are acquired at $b_d = \pm b_s$. Normalizing by a datapoint acquired with no diffusion weighting $b_s = 0$ removes relaxation effects. This is a relative measure of exchange and is enough to provide image contrast in MRI, to look at time-varying processes, or to measure exchange rates (discussed below).

In our previous publication we developed the theory for obtaining the exchanging fraction, f, from $(\partial^2 I/\partial b_d^2)$, which for a two-site exchange model results in (17)

$$\begin{aligned} f &= \left(\frac{\partial^2 I}{\partial b_d^2}\Big|_{b_d=b}\right)\frac{e^{b_sD_s}}{\cosh(b_dD_d)D_d^2} \\ &= \left(\frac{\partial^2 I}{\partial b_d^2}\Big|_{b_d=0}\right)\frac{e^{b_sD_s}}{D_d^2} \end{aligned} \tag{S9}$$

where

$$D_s = \frac{(D_e + D_i)}{2};\ D_d = \frac{(D_e - D_i)}{2}. \tag{S10}$$

Fitting exchange parameters. Exchange rates can be estimated from the full DEXSY or the rapid measurement by repeating the measurement with multiple mixing times which span the exchange process. Exchange parameters can be determined assuming exchange between diffusion environments is governed by a first-order rate law of the form $df_{i,e}/dt = k_{i,e}f_{i,i} - k_{e,i}f_{e,i}$ with rate constants $k_{i,e}$ and $k_{e,i}$ (26). The data we present calls for a nonzero initial condition; $f_{i,e}(t_m = 0) = f_{i,e0}$ (discussed below). The resulting two-site exchange model is:

$$\begin{aligned} f_{i,e}(t) = f_{e,i}(t) = \frac{f(t)}{2} &= \left(\frac{f_ek_{e,i}}{k_{e,i}+k_{i,e}} - f_{e,i0}\right)\left(1 - e^{-(k_{i,e}+k_{e,i})t}\right) + f_{e,i0} \\ &= \left(\frac{f_ik_{i,e}}{k_{i,e}+k_{e,i}} - f_{i,e0}\right)\left(1 - e^{-(k_{e,i}+k_{i,e})t}\right) + f_{i,e0}, \end{aligned} \tag{S11}$$

with equilibrium fractions f_e and f_i. With either the full DEXSY or the rapid measurement, exchanging fractions as a function of mixing time can be fit with a 3-parameter model of the form

$$f(t_m) = (f_{SS} - f_0)\left[1 - e^{-kt_m}\right] + f_0 \tag{S12}$$

to estimate the initial exchange fraction $f_0 = 2f_{i,e0}$, the steady-state exchange fraction $f_{SS} = \frac{2f_ik_{i,e}}{k_{i,e}+k_{e,i}}$, and the characteristic exchange rate $k = k_{i,e} + k_{e,i}$ (called the apparent exchange rate, AXR, in the text).

The data we present calls for a nonzero initial condition. A previous study of T_2–T_2 exchange in a polymer–solvent system near the glass transition also observed finite exchange when $t_m \approx 0$ (29). Models have shown significant exchange during the encoding periods τ can lead to exchange peaks at $t_m = 0$ (30).

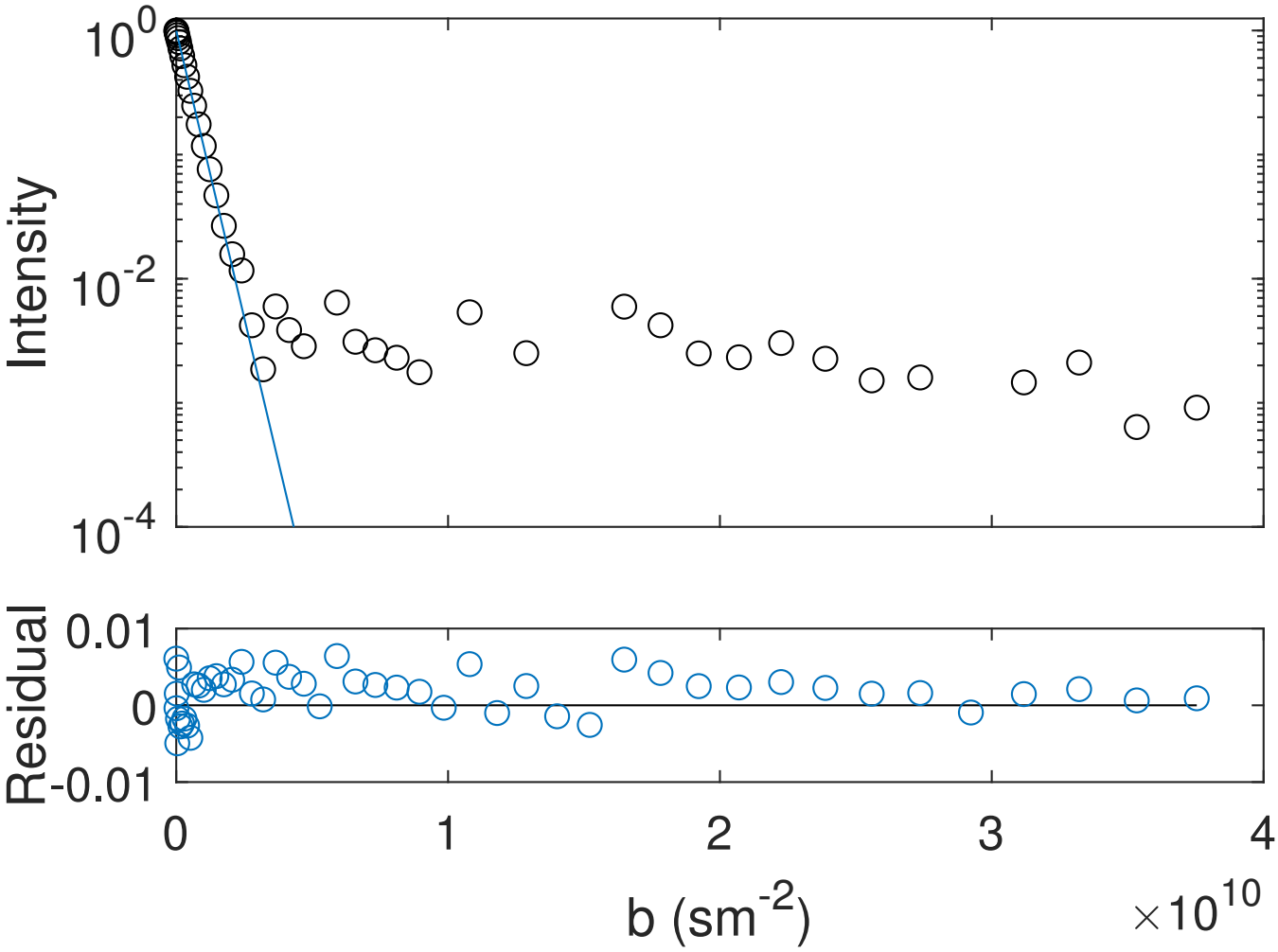

Fig. S1. 1-D diffusion data, single exponential fit and residuals for aCSF at 25C, 50 points. A fit of the first 15 points, attenuating the signal to $I/I_0 = 0.1$, provides $D_0 = 2.153 \pm 0.014 \times 10^{-9}\ \mathrm{m}^2/\mathrm{s}$ from three measurements.

Table S1. DEXSY Phase Cycles

ϕ_1	ϕ_2	ϕ_3	ϕ_4	ϕ_5	ϕ_6	ϕ_{rec}
0	$+\pi/2$	0	0	$+\pi/2$	$\pi/2$	π
π	$-\pi/2$	0	0	$+\pi/2$	$\pi/2$	0
0	$+\pi/2$	π	0	$+\pi/2$	$\pi/2$	0
π	$-\pi/2$	π	0	$+\pi/2$	$\pi/2$	π
0	$+\pi/2$	0	π	$-\pi/2$	$\pi/2$	0
π	$-\pi/2$	0	π	$-\pi/2$	$\pi/2$	π
0	$+\pi/2$	π	π	$-\pi/2$	$\pi/2$	π
π	$-\pi/2$	π	π	$-\pi/2$	$\pi/2$	0

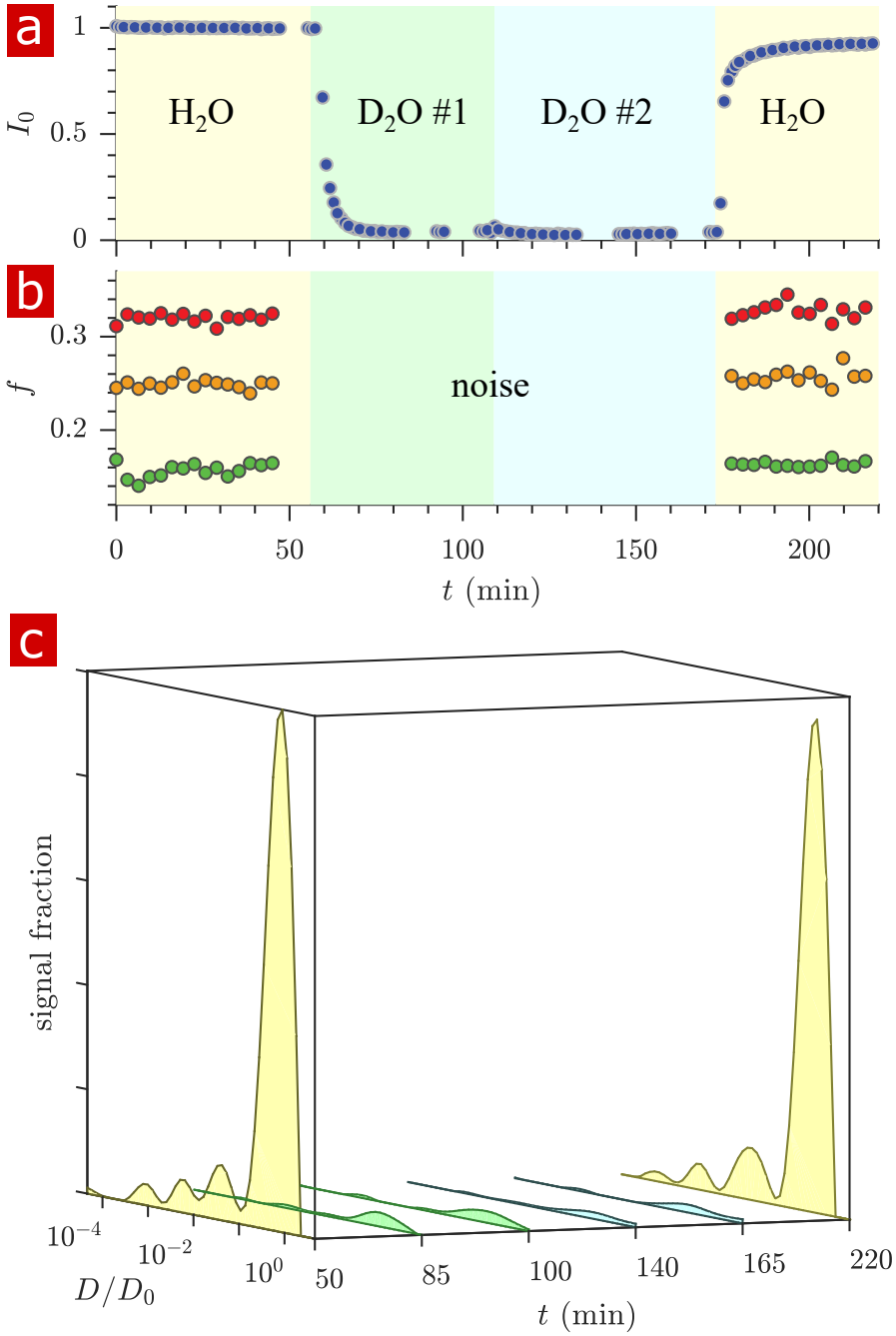

Fig. S2. Timecourse study of D_2O wash, in which the sample was washed in two steps from aCSF to aCSF made with deuterated water, showing a) the proton signal intensity from the rapid exchange measurement data normalized to remove T_1 effects at different mixing times and b) exchanging fractions from rapid measurements with $t_m = 0.2$ (blue), 4 (red), and 20 ms (orange). 1-D diffusion measurements were performed at points throughout the time-course (seen as breaks in the data in (a) and (b)) and distributions are presented as signal fractions ($P(D) \times I_0$) in (c). All distribution peaks decreased after washing with D_2O indicating that signal is primarily composed of water.

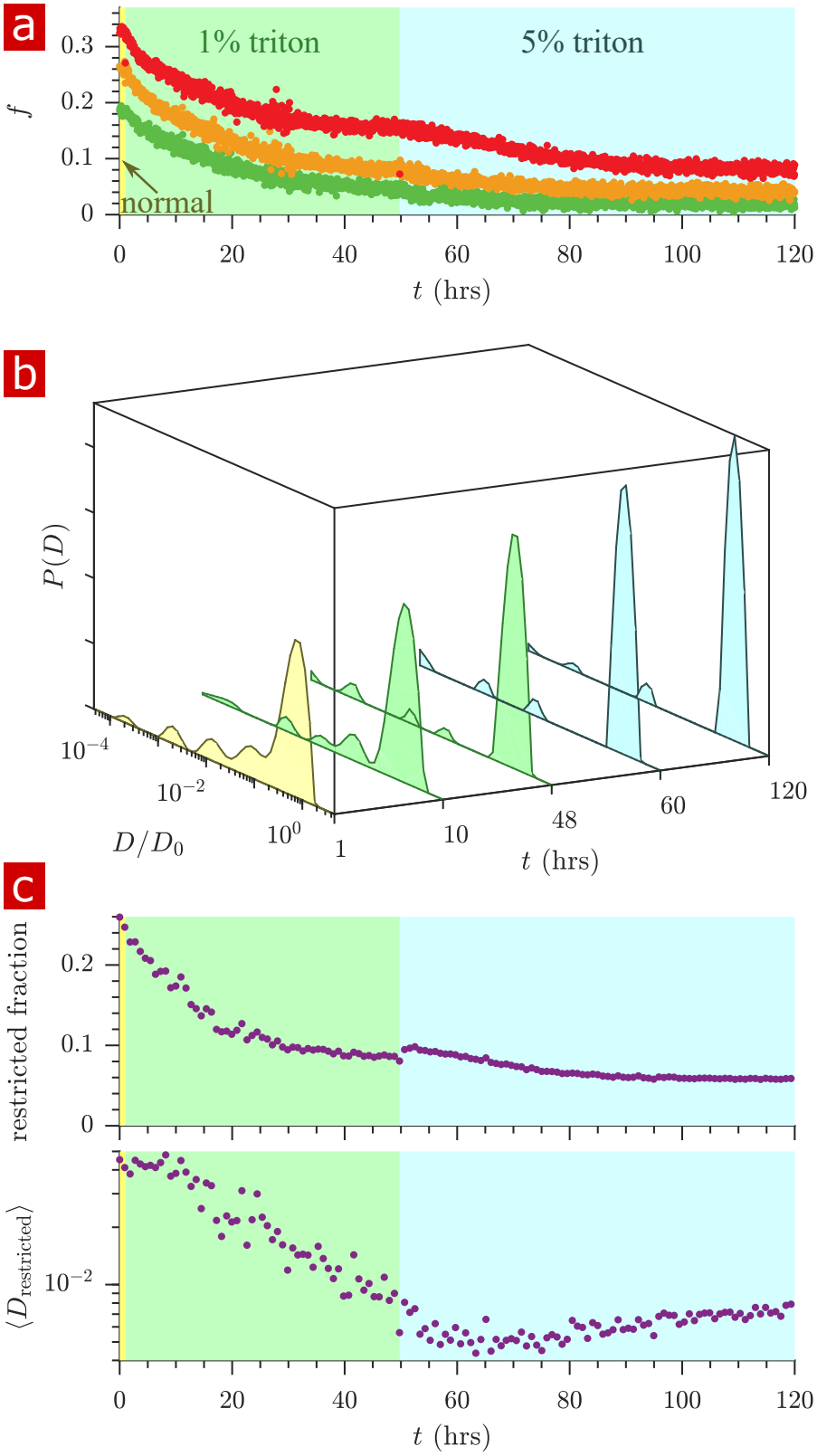

Fig. S3. Timecourse study of Triton X delipidation, in which the sample was washed to aCSF with 1% Triton X, and then 5% Triton X showing a) exchanging fractions from rapid measurements with $t_m = 0.2$ (green), 4 (orange), and 20 ms (red), b) representative distributions throughout the timecourse, and c) the fraction and mean diffusion coefficient of signal arising from restricted water ($D/D_0 < 0.17$). A bump in the restricted fraction seen upon addition of the 5% Triton is due to the Triton X itself which forms 5 nm micelles (31). The loss of the restricted diffusion peaks and the decrease in the exchanging fractions shows that membranes are the cause of water restriction.

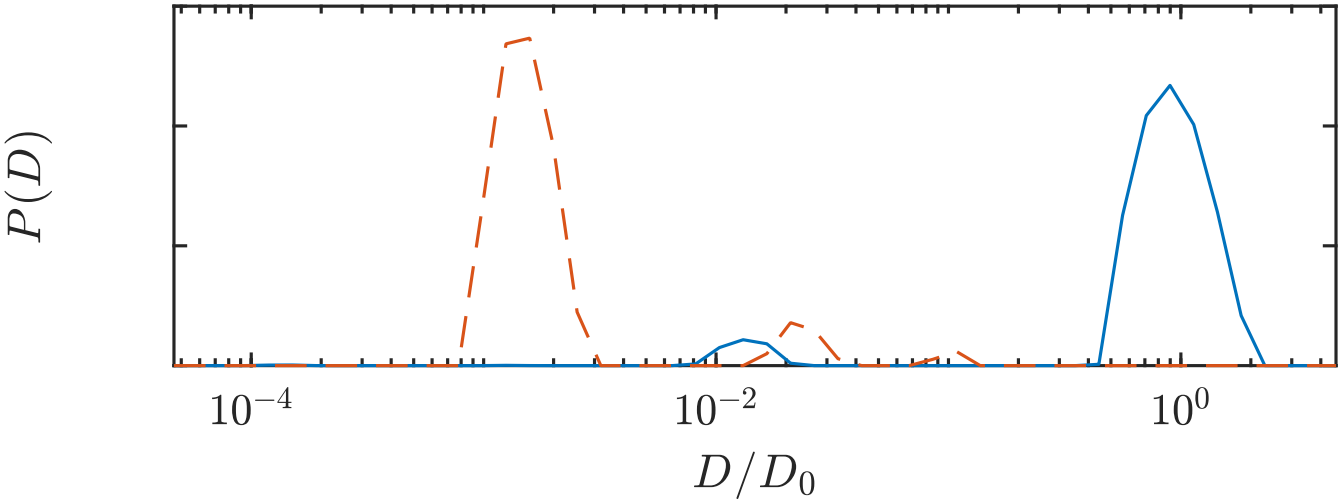

Fig. S4. Diffusion coefficient distributions of 5% Triton X in aCSF (solid blue line) and pure triton (dashed red line). The standard diffusion measurement protocol (43 pts. $\tau = 0.5 \rightarrow 6.6$) was used. The 5% Triton X shows an additional peak at $D/D_0 = 0.013$ due to formation of 5 nm micelles (31). Pure Triton X shows a major diffusion coefficient component at $D/D_0 = 0.001$ 5% Triton is due to the Triton X itself, indicating that signal from protons on Triton are measured.

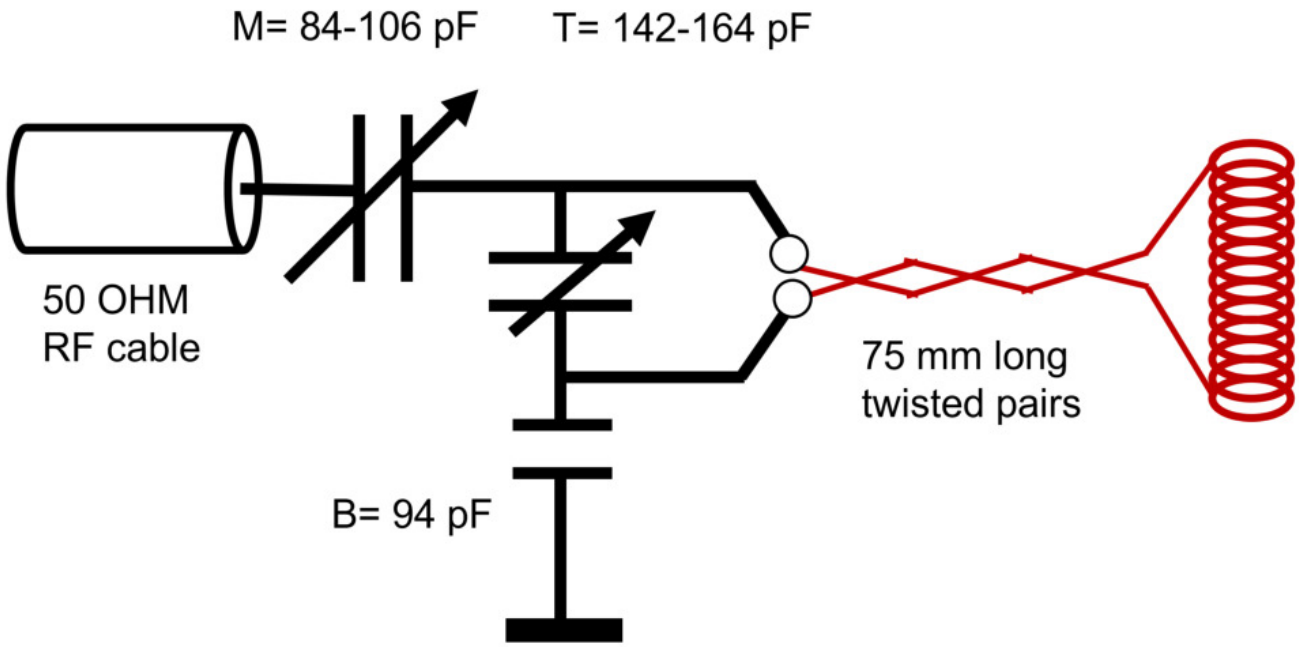

Fig. S5. Drawing of the circuit for the RF showing the capacitance of the tune (T), match (M), and balance (B). Note a single wrapping of the solenoid was drawn rather than the actual double-wrap for visual simplicity

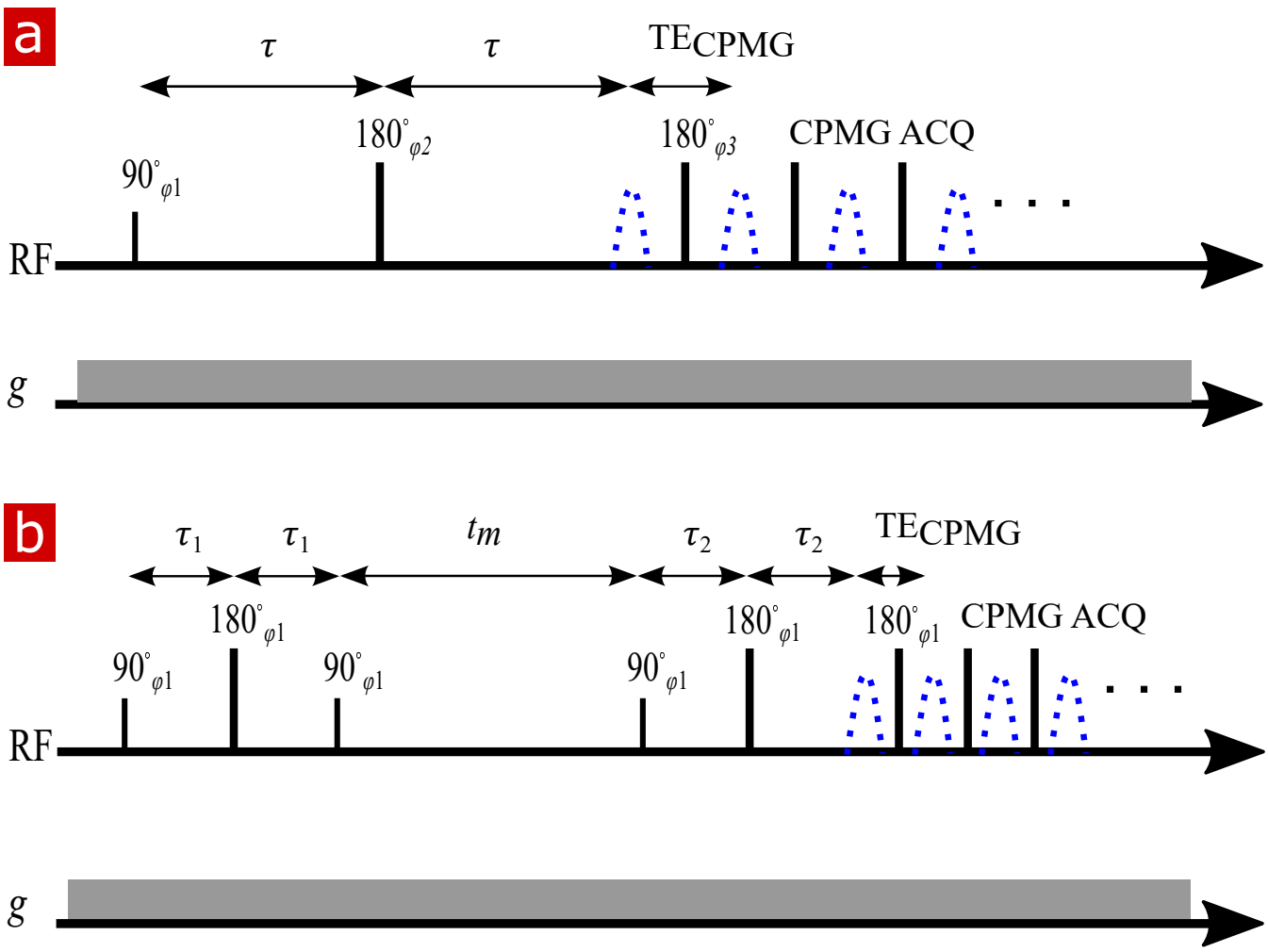

Fig. S6. (a) Spin echo pulse sequence for measuring diffusion with a static gradient. τ is varied to control b. (b) DEXSY pulse sequence for measuring exchange with a static gradient. The two SE encoding blocks with τ_1 and τ_2, varied independently to control b_1 and b_2, are separated by t_m. Signal is acquired in a CPMG train for both (a) and (b).

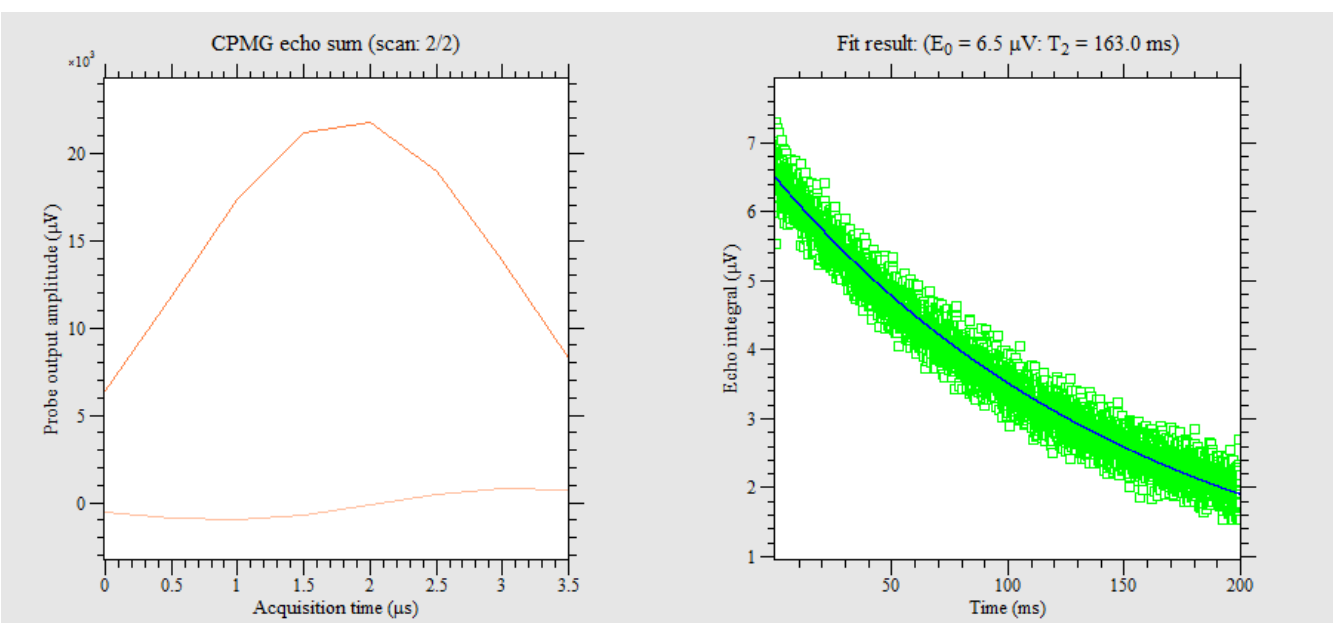

Fig. S7. representative Carr-Purcell-Meiboom-Gill (CPMG) T_2 measurement (10s repetition time (TR), 8000 echoes) on fixed spinal cord showing the echo shape (real signal phased maximum and imaginary signal phased to zero) on the left and real signal decay and exponential fit on the right. Figures are output from the Prospa (Magritek, New Zealand) software.

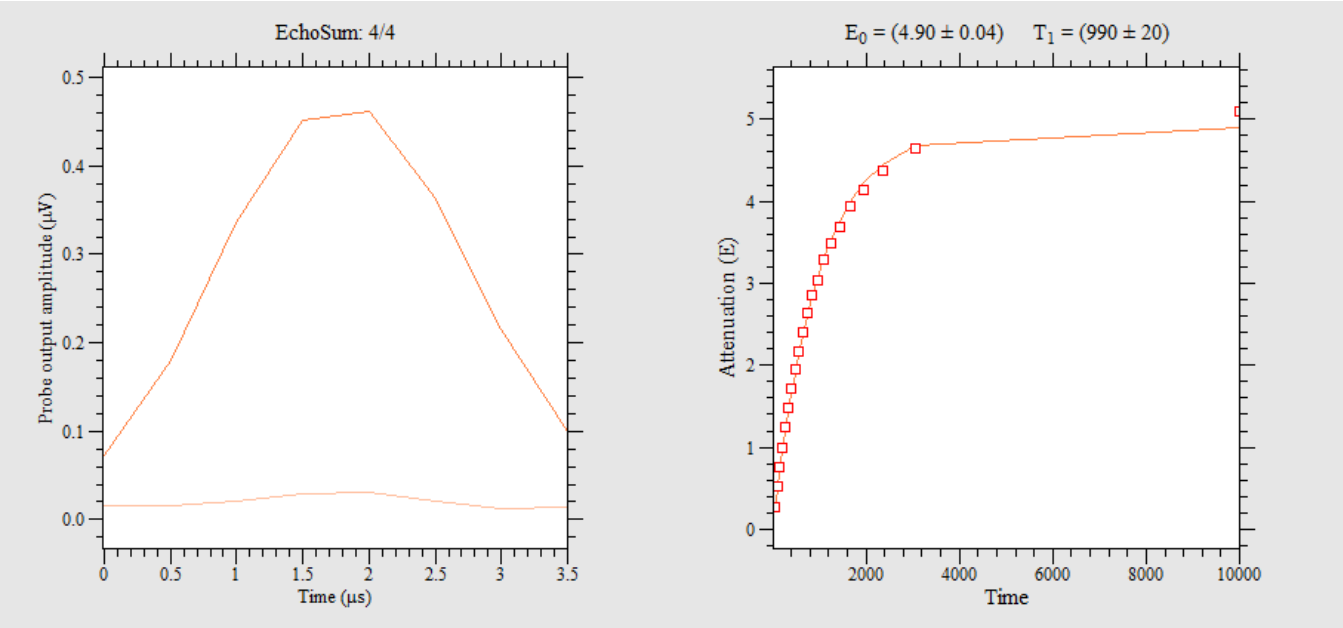

Fig. S8. representative saturation recovery T_1 measurement (1s TR, 21 recovery time pts. logarithmically spaced from 50 ms to 10s) on fixed spinal cord showing the echo shape (real signal phased maximum and imaginary signal phased to zero) on the left and real signal recovery and exponential fit on the right. Figures are output from the Prospa (Magritek, New Zealand) software.

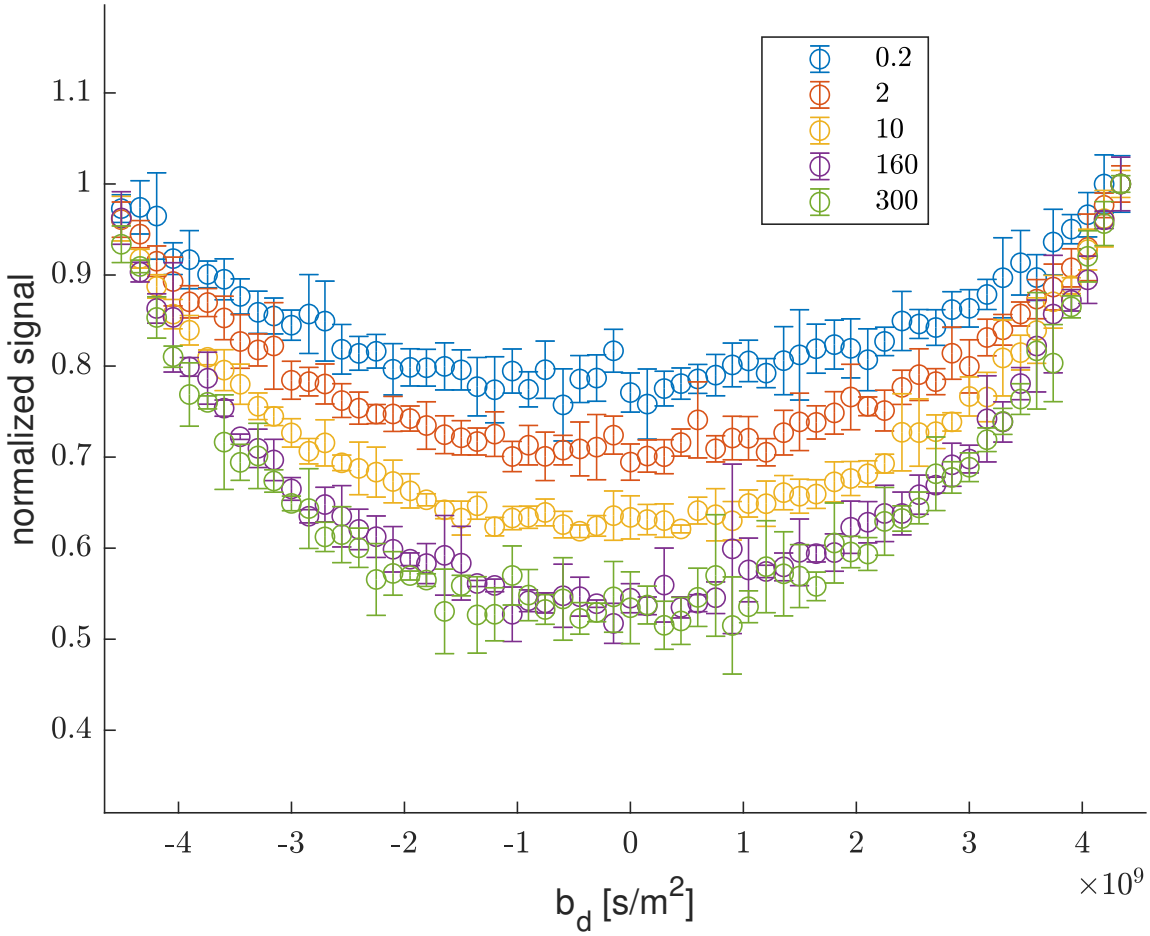

Fig. S9. The curvature along slices of $b_s = 4500\ \mathrm{s/mm^2}$ as a function of b_d highlighting the increase in the depth of the curvature with increasing t_m, shown in figure legend. The increased depth is due to increased exchange (17, 28)

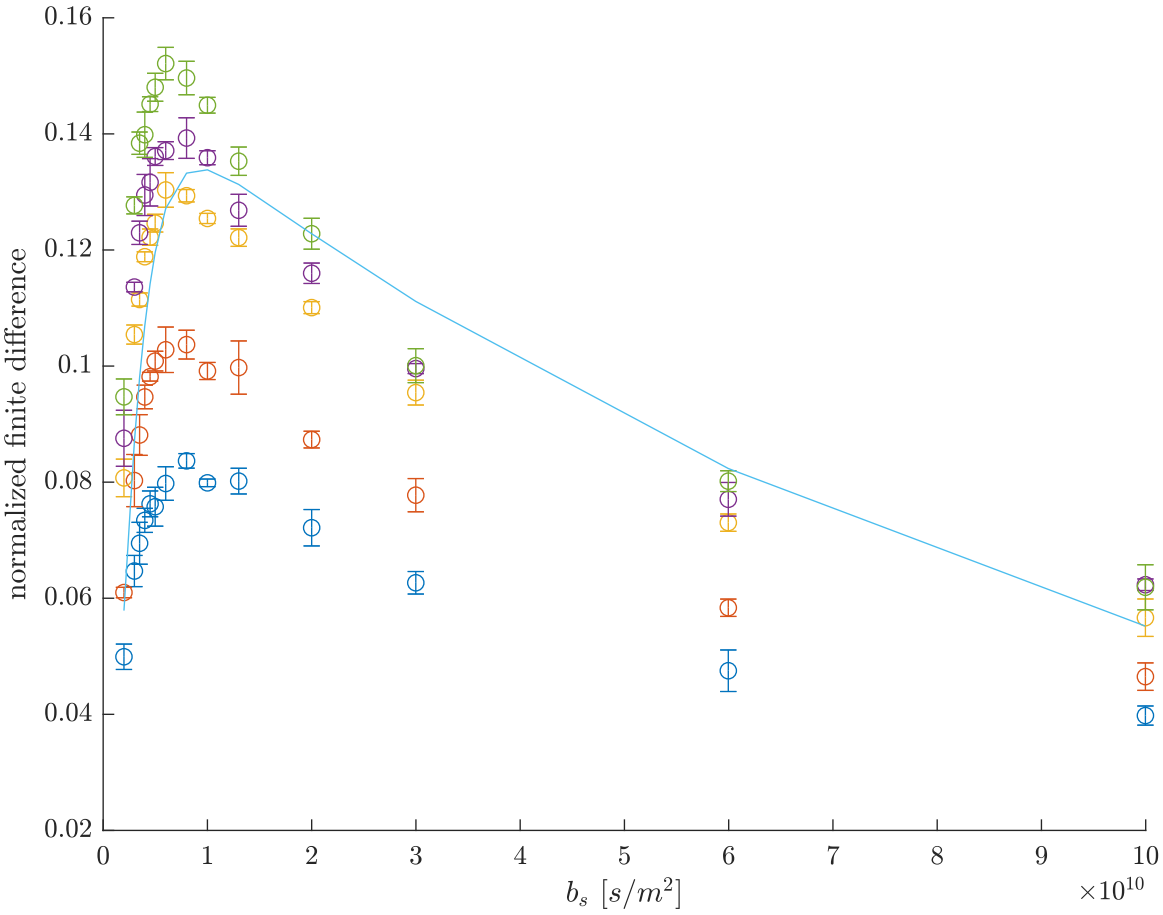

Fig. S10. The finite difference as a function of b_s, showing the optimal b_s for measuring the largest curvature response as occurring near $b_s = 6000\ \mathrm{s/mm^2}$. The line is a prediction of the finite difference for a two-site system, from Eq. 8 in Ref. (17) using $f = 0.15$, $D_e = 10^{-9}$, and $D_i = 10^{-11}\ \mathrm{s/mm^2}$.

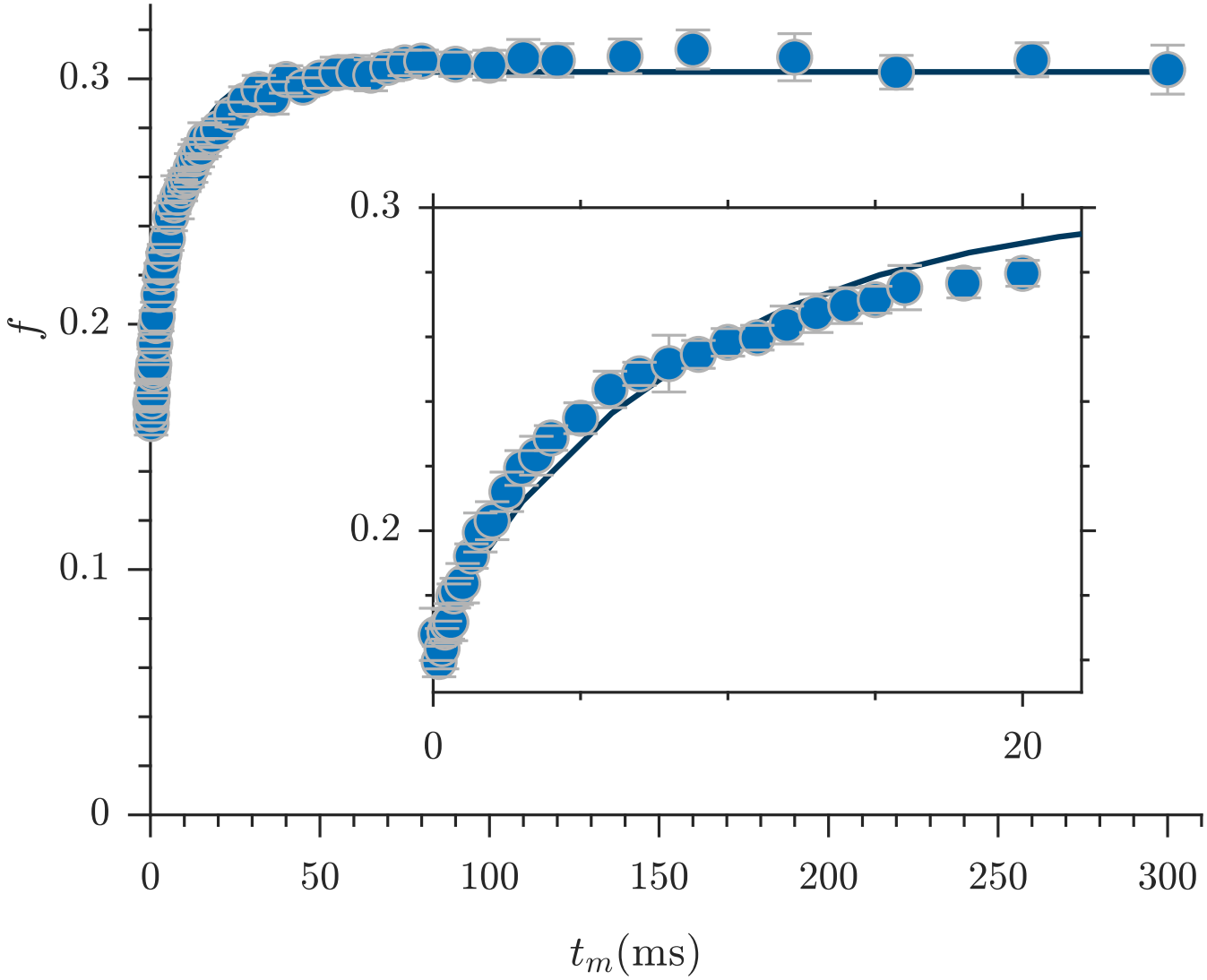

Fig. S11. High temporal resolution exchange rate measurement from the rapid measurement with $b_s = 4500\ \mathrm{s/mm^2}$ and 53 t_m points between 0.1 and 300 ms. First order rate model fits estimate AXR=113.7 ± 5.2 ms (solid line).

Bibliography

1. MD Hurlimann, KG Helmer, TM Deswiet, and PN Sen. Spin echoes in a constant gradient and in the presence of simple restriction. *Journal of Magnetic Resonance*, 113:260–264, 1995.
2. Erwin L Hahn. Spin echoes. *Physical review*, 80(4):580, 1950.
3. Herman Y Carr and Edward M Purcell. Effects of diffusion on free precession in nuclear magnetic resonance experiments. *Physical review*, 94(3):630, 1954.
4. Donald E Woessner. Effects of diffusion in nuclear magnetic resonance spin-echo experiments. *The Journal of Chemical Physics*, 34(6):2057–2061, 1961.
5. John E Tanner. Transient diffusion in a system partitioned by permeable barriers. application to nmr measurements with a pulsed field gradient. *The Journal of Chemical Physics*, 69(4):1748–1754, 1978.
6. Denis Le Bihan, Eric Breton, Denis Lallemand, Philippe Grenier, Emmanuel Cabanis, and Maurice Laval-Jeantet. Mr imaging of intravoxel incoherent motions: application to diffusion and perfusion in neurologic disorders. *Radiology*, 161(2):401–407, 1986.
7. Thomas M de Swiet and Pabitra N Sen. Decay of nuclear magnetization by bounded diffusion in a constant field gradient. *The Journal of chemical physics*, 100(8):5597–5604, 1994.
8. Richard Conable Wayne and Robert M Cotts. Nuclear-magnetic-resonance study of self-diffusion in a bounded medium. *Physical Review*, 151(1):264, 1966.
9. Baldwin Robertson. Spin-echo decay of spins diffusing in a bounded region. *Physical Review*, 151(1):273, 1966.
10. CH Neuman. Spin echo of spins diffusing in a bounded medium. *The Journal of Chemical Physics*, 60(11):4508–4511, 1974.
11. KJ Carlton, MR Halse, and John H Strange. Diffusion-weighted imaging of bacteria colonies in the strafi plane. *Journal of Magnetic Resonance*, 143(1):24–29, 2000.
12. Sarah L Codd and Paul T Callaghan. Spin echo analysis of restricted diffusion under generalized gradient waveforms: planar, cylindrical, and spherical pores with wall relaxivity. *Journal of Magnetic Resonance*, 137(2):358–372, 1999.
13. Brett N Ryland and Paul T Callaghan. Spin echo analysis of restricted diffusion under generalized gradient waveforms for spherical pores with relaxivity and interconnections. *Israel journal of chemistry*, 43(1-2):1–7, 2003.
14. Carin Malmborg, Daniel Topgaard, and Olle Söderman. Nmr diffusometry and the short gradient pulse limit approximation. *Journal of Magnetic Resonance*, 169(1):85–91, 2004.
15. Alexandru V Avram, Evren Özarslan, Joelle E Sarlls, and Peter J Basser. In vivo detection of microscopic anisotropy using quadruple pulsed-field gradient (qpfg) diffusion mri on a clinical scanner. *Neuroimage*, 64:229–239, 2013.
16. John Crank. *The mathematics of diffusion*. Oxford university press, 1979.
17. Teddy X Cai, Dan Benjamini, Michal E Komlosh, Peter J Basser, and Nathan H Williamson. Rapid detection of the presence of diffusion exchange. *Journal of Magnetic Resonance*, 297:17–22, 2018.
18. D.G. Rata, F. Casanova, J. Perlo, D.E. Demco, and B. Blümich. Self-diffusion measurements by a mobile single-sided nmr sensor with improved magnetic field gradient. *Journal of Magnetic Resonance*, 180(2):229 – 235, 2006. ISSN 1090-7807. doi: https://doi.org/10.1016/j.jmr.2006.02.015.
19. Saul Meiboom and David Gill. Modified spin-echo method for measuring nuclear relaxation times. *Review of scientific instruments*, 29(8):688–691, 1958.
20. Federico Casanova, Juan Perlo, and Bernhard Blümich. *Single-sided NMR*. Springer, 2011.
21. Martin D Hürlimann. Diffusion and relaxation effects in general stray field nmr experiments. *Journal of magnetic resonance*, 148(2):367–378, 2001.
22. Ruiliang Bai, Andreas Klaus, Tim Bellay, Craig Stewart, Sinisa Pajevic, Uri Nevo, Hellmut Merkle, Dietmar Plenz, and Peter J Basser. Simultaneous calcium fluorescence imaging and mr of ex vivo organotypic cortical cultures: a new test bed for functional mri. *NMR in Biomedicine*, 28(12):1726–1738, 2015.
23. Jan Watzlaw, Stefan Glöggler, Bernhard Blümich, Wilfried Mokwa, and Uwe Schnakenberg. Stacked planar micro coils for single-sided nmr applications. *Journal of Magnetic Resonance*, 230: 176–185, 2013.
24. Alexandre A Khrapitchev and Paul T Callaghan. Double pgse nmr with stimulated echoes: phase cycles for the selection of desired encoding. *Journal of Magnetic Resonance*, 152(2):259–268, 2001.
25. Oliver Neudert, Siegfried Stapf, and Carlos Mattea. Diffusion exchange nmr spectroscopy in inhomogeneous magnetic fields. *Journal of Magnetic Resonance*, 208(2):256–261, 2011.
26. K. E. Washburn and P. T. Callaghan. Tracking pore to pore exchange using relaxation exchange spectroscopy. *Physical Review Letters*, 97:175502, Oct 2006.
27. P. T. Callaghan and I. Furó. Diffusion-diffusion correlation and exchange as a signature for local order and dynamics. *The Journal of Chemical Physics*, 120(8):4032–4038, 2004.
28. Ruobing Song, Yi-Qiao Song, Muthusamy Vembusubramanian, and Jeffrey L. Paulsen. The robust identification of exchange from t2–t2 time-domain features. *Journal of Magnetic Resonance*, 265: 164 – 171, 2016. ISSN 1090-7807.
29. Nathan H Williamson, April M Dower, Sarah L Codd, Amber L Broadbent, Dieter Gross, and Joseph D Seymour. Glass dynamics and domain size in a solvent-polymer weak gel measured by multidimensional magnetic resonance relaxometry and diffusometry. *Physical review letters*, 122(6):068001, 2019.
30. L. M. Schwartz, D. L. Johnson, J. Mitchell, T. C. Chandrasekera, and E. J. Fordham. Modeling two-dimensional magnetic resonance measurements in coupled pore systems. *Phys. Rev. E*, 88: 032813, Sep 2013. doi: 10.1103/PhysRevE.88.032813.
31. H Hasko Paradies. Shape and size of a nonionic surfactant micelle. triton x-100 in aqueous solution. *The Journal of Physical Chemistry*, 84(6):599–607, 1980.